

LANGLEY
GRANT
11-02-CR
510573

S. AHMED
J.C. TANNEHILL

82P

OCTOBER 1990

(NASA-CR-187343) NUMERICAL COMPUTATION OF
VISCOUS FLOW ABOUT UNCONVENTIONAL AIRFOIL
SHAPES Final Report (Iowa State Univ. of
Science and Technology) 82 p

N91-10019

CSCL 01A

Unclass

63/02 0310573

FINAL REPORT

NUMERICAL COMPUTATION OF VISCOUS FLOW ABOUT UNCONVENTIONAL AIRFOIL SHAPES

Submitted to:

National Aeronautics and Space Administration
Langley Research Center
Hampton, Virginia
NASA Grant NAG-1-645

ISU-ERI-Ames-91-110
ERI Project 1874
CFD 24

ENGINEERING RESEARCH INSTITUTE
IOWA STATE UNIVERSITY
AMES, IOWA 50011 USA

**S. AHMED
J.C. TANNEHILL**

OCTOBER 1990

FINAL REPORT

**NUMERICAL COMPUTATION OF
VISCOUS FLOW ABOUT
UNCONVENTIONAL AIRFOIL SHAPES**

Submitted to:

**National Aeronautics and Space Administration
Langley Research Center
Hampton, Virginia
NASA Grant NAG-1-645**

**ISU-ERI-Ames-91-110
ERI Project 1874
CFD 24**

**ENGINEERING RESEARCH INSTITUTE
IOWA STATE UNIVERSITY
AMES, IOWA 50011 USA**

TABLE OF CONTENTS

SUMMARY	iv
NOMENCLATURE	v
CHAPTER 1. INTRODUCTION	1
CHAPTER 2. GOVERNING EQUATIONS	5
CHAPTER 3. TURBULENCE MODEL	11
Development of a New Turbulence Model for Wall Bounded Shear Flows	11
Wake Model	17
CHAPTER 4. NUMERICAL METHOD	22
First-order Scheme	23
Second-order TVD Scheme	24
Implicit Algorithm	25
Computational Grid	28
CHAPTER 5. RESULTS AND DISCUSSIONS	31
NACA 0012 Airfoil	31
RAE 2822 Airfoil	33

Integrated Technology Airfoil	50
CHAPTER 6. CONCLUDING REMARKS	63
BIBLIOGRAPHY	64
ACKNOWLEDGEMENTS	67
APPENDIX A. TURBULENT DIFFUSION	68
APPENDIX B. NONEQUILIBRIUM EFFECTS IN THE INNER LAYER	70

SUMMARY

A new two-dimensional computer code has been developed to analyze the viscous flow around unconventional airfoils at various Mach numbers and angles of attack. The Navier-Stokes equations are solved using an implicit, upwind, finite-volume scheme. Both laminar and turbulent flows can be computed. A new nonequilibrium turbulence closure model was developed for computing turbulent flows. This two-layer eddy viscosity model was motivated by the success of the Johnson-King model in separated flow regions. The influence of history effects are described by an ordinary differential equation developed from the turbulent kinetic energy equation. The performance of the present code has been evaluated by solving the flow around three airfoils using the Reynolds time-averaged Navier-Stokes equations. Excellent results were obtained for both attached and separated flows about the NACA 0012 airfoil, the RAE 2822 airfoil, and the Integrated Technology A 153W airfoil. Based on the comparison of the numerical solutions with the available experimental data, it is concluded that the present code in conjunction with the new nonequilibrium turbulence model gives excellent results.

NOMENCLATURE

A	damping length constant
\tilde{A}	Roe-averaged flux vector Jacobian matrix associated with \hat{F}
\tilde{B}	Roe-averaged flux vector Jacobian matrix associated with \hat{G}
a	speed of sound
b	wake width
c	airfoil chord
C_d	drag coefficient
C_f	skin-friction coefficient
C_l	lift coefficient
C_m	quarter-chord moment coefficient
C_n	normal force coefficient
C_p	surface-pressure coefficient
D	$D^+ - D^-$
D^\pm	portion of \tilde{A} associated with positive/ negative eigenvalues
dF	MINMOD of flux difference
E	$E^+ - E^-$
E^\pm	portion of \tilde{B} associated with positive/ negative eigenvalues
E_t	total energy per unit volume

e	specific internal energy
F, G	flux vectors
F_c	turbulence velocity scale correction in the inner layer
h	instantaneous enthalpy per unit mass
\bar{h}	mass-averaged h
I	identity matrix
J	Jacobian
K	Clauser constant
\bar{k}	mean turbulent kinetic energy per unit mass
M	Mach number
N	viscous Jacobian matrix
n	time index
p	instantaneous thermodynamic pressure
\bar{p}	mean thermodynamic pressure
Pr	Prandtl number
Pr_t	turbulent Prandtl number
\bar{Q}	vector of conservative variables
\bar{R}, \bar{S}	viscous stress vector
R	matrix of right eigenvectors
R^{-1}	matrix of left eigenvectors
Re	Reynolds number based on airfoil chord
T	instantaneous temperature
\bar{T}	mass-averaged temperature

t	time
U_ϵ	boundary layer edge velocity
u	instantaneous velocity component in the x direction
u_τ	friction velocity
\bar{u}	mass-averaged u
v	instantaneous velocity component in the y direction
V	lateral convection velocity
V_0	maximum lateral convection velocity
\bar{v}	mass-averaged v
w	wake velocity defect
x, y	coordinates in physical space
y^+	nondimensionalized boundary layer distance
α	angle of attack
γ	ratio of specific heats
$\bar{\gamma}$	Klebanoff intermittency
Δ, ∇	forward / backward difference operator
δ	boundary layer thickness
δ^*	boundary layer displacement thickness
θ	boundary layer momentum thickness
κ	von Karman constant
λ	coefficient of thermal conductivity

μ	coefficient of molecular viscosity
μ_t	coefficient of eddy viscosity
ν	coefficient of kinematic viscosity
ν_t	coefficient of kinematic eddy viscosity
ξ, η	computational axis
ρ	instantaneous density
$\bar{\rho}$	mean density
$-\rho u_i' u_j'$	Reynolds stress
$\hat{\tau}$	total stress
Φ	MINMOD operator
ϕ	accuracy parameter
ω	weighting for central/upwind differencing
ϖ	vorticity

subscripts

a	asymptotic
e	edge, equilibrium
i	inner, ξ -index
j	η -index
max_F	condition where $y \mid \varpi \mid$ is maximum
m	condition where moment of turbulent shear is maximum

max	condition at the location of maximum turbulent shear
o	outer
t	turbulent
∞	freestream conditions
w	wake, wall

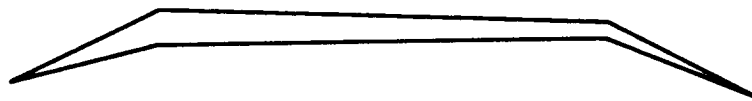
CHAPTER 1. INTRODUCTION

In the transonic regime, the viscous flow about airfoils at angle of attack is often complex. These flows may include a few or all of the following: shock waves, strong shock wave/boundary layer interactions, separation bubbles and regions of massive separation [1]. The occurrence of these adverse flow behaviors is strongly influenced by the airfoil geometry. In recent years, airfoil profiles have been dramatically altered to improve airfoil characteristics [2,3,4,5,6,7]. These changes include leading- and trailing-edge flap deflections, blunt trailing edges, laminar flow airfoils and supercritical-type airfoils. Geometric features promoting adverse flow patterns are: 1) small leading edge radii, 2) surface and surface slope discontinuities, and 3) nonstandard camber or thickness distributions. In the present work, airfoils with these geometric features have been referred to as unconventional airfoils. Some typical unconventional airfoil shapes are depicted in Figure 1.1.

The occurrence of laminar flow around airfoils is an exception. Boundary layers on aircraft wings are predominantly turbulent. With this in mind, the objective of the present work is to compute the turbulent flow about unconventional airfoils at subsonic and transonic Mach numbers. The Navier-Stokes solver developed by Cox [8] is used to solve the Reynolds time-averaged equations. It is well known that the success of a prediction method for turbulent flows depends to a large extent on the



BLUNT TRAILING-EDGES



SURFACE-SLOPE DISCONTINUITIES



SMALL LEADING-EDGE RADIUS



NON-STANDARD CAMBER AND
THICKNESS DISTRIBUTIONS

Figure 1.1: Typical unconventional airfoil shapes

choice of the turbulence model [9]. Although progress has been made towards the development of a universal turbulence model for use in turbulent flow calculations, the goal has not been reached yet. In many of the noncomplex flows considered in the past, such as attached wall-bounded flows with zero or mild pressure gradients, calculations based on simple algebraic turbulence models have been shown to be within the measurement precision of experiments. The main reason for the success of an algebraic eddy viscosity model is that most of the basic fluid flows used as test cases are nearly in a state of self-preservation or of local equilibrium in the sense that generation of Reynolds stress is in complete balance with its destruction [10]. Turbulent flows usually take up self-preserving forms if permitted by the boundary conditions. Near a solid surface in the so called inner layer, the velocity scale of turbulence depends not only on the shear stress transmitted through the layer to the surface, but also on the transport of Reynolds stress. In this region, the largest stress containing eddies have a wavelength of the order of the distance from the surface. Thus the turbulence length scale in the inner layer may be taken to be proportional to the distance from the surface. On the other hand, the outer layer is dominated by large eddies [10] that have considerably longer life times. As a result, history effects are much more important in the outer part of a turbulent boundary layer.

It was argued by Bradshaw and Ferriss [11] that the turbulent shear stress $-\overline{u'v'}$ is closely related to the turbulent kinetic energy and that the latter is governed by the turbulent kinetic energy equation. The success of the Johnson-King model [12] is a testimony to the above mentioned findings of Bradshaw and Ferriss. The Johnson-King model performs quite well in regions of adverse pressure gradients and separation

but it does not always do as well in cases where simpler equilibrium (algebraic) eddy viscosity models produce good results. It may be possible that this model overemphasizes nonequilibrium effects in near equilibrium turbulent flows.

As a result of the above observations, an effort was undertaken to develop a new turbulence model from a variation of the turbulent kinetic energy equation [13]. This two-layer model is developed directly from the available experimental observations of both attached and separated flows. An ordinary differential equation, derived from the turbulent kinetic energy equation, is used to describe the so called history effects of convection and diffusion of turbulent shear stress. In view of this, the model is not simply an eddy viscosity model, but also contains the desirable features of a Reynolds stress model. Although it bears a strong resemblance to the Johnson-King model, the present nonequilibrium turbulence model is unique. In addition, it is much easier to incorporate into a Navier-Stokes solver than the Johnson-King model since it does not involve any iteration.

The performance of the new turbulence model is illustrated through comparisons with experimental results for turbulent flows about three different airfoils: the NACA 0012 airfoil, the RAE 2822 airfoil and the Integrated Technology A 153W airfoil.

CHAPTER 2. GOVERNING EQUATIONS

Turbulence can be regarded as the time-dependent solution of the Navier-Stokes equations resulting from all the nonlinear processes. These nonlinear processes include the instabilities within the equations and the flowfield disturbances. Unfortunately, the association of very small length scales of the turbulence eddies along with small time scales prohibit the numerical solution of the complete Navier-Stokes equations for complex problems on present day computers. Nonetheless, useful results can be obtained from numerical solutions of intelligently simplified versions of the Navier-Stokes equations. Currently, the main thrust of engineering calculations are based on the Reynolds time-averaged equations [14]. These equations can be obtained by using Favre's mass-weighted averaging as

$$\frac{\partial \bar{\rho}}{\partial t} + \frac{\partial}{\partial x_j} (\bar{\rho} \tilde{u}_j) = 0 \quad (2.1)$$

$$\frac{\partial}{\partial t} (\bar{\rho} \tilde{u}_i) + \frac{\partial}{\partial x_j} [\bar{\rho} \tilde{u}_i \tilde{u}_j + \delta_{ij} \bar{p} - (\bar{\tau}_{ij} - \overline{\rho u_i' u_j'})] = 0 \quad (2.2)$$

$$\frac{\partial \bar{E}_t}{\partial t} + \frac{\partial}{\partial x_j} [\tilde{u}_j (\bar{p} + \bar{E}_t) + \bar{q}_j + \overline{\rho u_j' h'} - \tilde{u}_i (\bar{\tau}_{ij} - \overline{\rho u_i' u_j'})] = 0 \quad (2.3)$$

where

$$u_i(x_i, t) = \bar{u}_i(x_i) + u_i'(x_i, t)$$

$$h(x_i, t) = \bar{h}(x_i) + h'(x_i, t)$$

$$T(x_i, t) = \bar{T}(x_i) + T'(x_i, t)$$

$$H(x_i, t) = \bar{H}(x_i) + H'(x_i, t)$$

$$\rho(x_i, t) = \bar{\rho}(x_i) + \rho'(x_i, t)$$

$$p(x_i, t) = \bar{p}(x_i) + p'(x_i, t)$$

$$\bar{u}_i = \frac{\overline{\rho u_i}}{\bar{\rho}}$$

$$\bar{h} = \frac{\overline{\rho h}}{\bar{\rho}}$$

$$\bar{T} = \frac{\overline{\rho T}}{\bar{\rho}}$$

$$\bar{H} = \frac{\overline{\rho H}}{\bar{\rho}}$$

and

$$\begin{aligned} \bar{\tau}_{ij} = & \mu \left[\left(\frac{\partial \bar{u}_i}{\partial x_j} - \frac{\partial \bar{u}_j}{\partial x_i} \right) - \frac{2}{3} \delta_{ij} \frac{\partial \bar{u}_k}{\partial x_k} \right] \\ & + \mu \left[\left(\frac{\partial u_i'}{\partial x_j} - \frac{\partial u_j'}{\partial x_i} \right) - \frac{2}{3} \delta_{ij} \frac{\partial u_k'}{\partial x_k} \right] \end{aligned} \quad (2.4)$$

$$\bar{q}_j = -\lambda \frac{\partial \bar{T}}{\partial x_j} \quad (2.5)$$

Here $\bar{\rho}$ is the mean density, \bar{u}_i is the mean velocity in the direction of x_i , \bar{E}_t is the mean total energy per unit volume, \bar{T} is the mean temperature, \bar{p} is the mean pressure, μ is the coefficient of molecular viscosity, λ is the coefficient of thermal conductivity and \bar{h} is the mean enthalpy per unit mass. It has been tacitly assumed that the fluctuations in μ and λ are negligible. In practice, the viscous terms involving the primed fluctuations are expected to be small and are candidates for being neglected on the basis of order of magnitude analysis [15]. Closure of the Reynolds time-averaged equations requires the specification of the turbulent stresses and heat flux terms. As in most turbulence models, the turbulent stresses are determined from the Boussinesq approximation

$$-\rho \overline{u_i' u_j'} = \mu_t \left[\left(\frac{\partial \bar{u}_i}{\partial x_j} + \frac{\partial \bar{u}_j}{\partial x_i} \right) - \frac{2}{3} \delta_{ij} \frac{\partial \bar{u}_k}{\partial x_k} \right] + \frac{2}{3} \delta_{ij} \bar{\rho} \bar{k} \quad (2.6)$$

where \bar{k} is the mean turbulent kinetic energy per unit mass; $\bar{\rho} \bar{k} = \frac{1}{2} \overline{\rho u_i' u_i'}$.

The apparent heat flux is related to the turbulent viscosity μ_t , mean flow variables, and the turbulent Prandtl number Pr_t by

$$-\rho \overline{u_i' h'} = C_p \frac{\mu_t}{Pr_t} \frac{\partial \bar{T}}{\partial x_i} \quad (2.7)$$

Experiments confirm that Pr_t (the ratio of the diffusivities for the turbulent transport of heat and momentum) is a well behaved function across the flow [15]. Generally Pr_t is close to 1 and a value of 0.9 is chosen in this report.

The above equations are nondimensionalized with respect to freestream speed of sound, density, temperature, coefficient of molecular viscosity and the independent

variables x_i are scaled by a characteristic length (the chord length in this case). Since a boundary-fitted coordinate system provides a significantly improved and easier means of implementing the surface boundary conditions, the foregoing equations are transformed from a Cartesian to a generalized nonorthogonal curvilinear coordinate system using the transformation

$$\begin{aligned} t &= t \\ \xi &= \xi(x_i) \\ \eta &= \eta(x_i) \\ \zeta &= \zeta(x_i) \end{aligned}$$

The resulting governing equations for a two-dimensional flow are written in vector notation as

$$\frac{\partial \hat{Q}}{\partial t} + \frac{\partial \hat{F}}{\partial \xi} + \frac{\partial \hat{G}}{\partial \eta} = \frac{M_\infty}{Re} \left[\frac{\partial \hat{R}}{\partial \xi} + \frac{\partial \hat{S}}{\partial \eta} \right] \quad (2.8)$$

where

$$\begin{aligned} \hat{F} &= y_\eta \bar{F} - x_\eta \bar{G} \\ \hat{G} &= -y_\xi \bar{F} + x_\xi \bar{G} \\ \hat{R} &= y_\eta \bar{R} - x_\eta \bar{S} \\ \hat{S} &= -y_\xi \bar{R} + x_\xi \bar{S} \\ \hat{Q} &= \frac{\bar{Q}}{J} \end{aligned} \quad (2.9)$$

and

$$\begin{aligned}
\bar{Q} &= \{\bar{\rho}, \bar{\rho}\bar{u}, \bar{\rho}\bar{v}, \bar{E}_t\}^T \\
\bar{F} &= \{\bar{\rho}\bar{u}, \bar{p} - \bar{\rho}\bar{u}^2, \bar{\rho}\bar{u}\bar{v}, (\bar{p} + \bar{E}_t)\bar{u}\}^T \\
\bar{G} &= \{\bar{\rho}\bar{v}, \bar{\rho}\bar{u}\bar{v}, \bar{p} - \bar{\rho}\bar{v}^2, (\bar{p} + \bar{E}_t)\bar{v}\}^T \\
\bar{R} &= \{0, \hat{\tau}_{xx}, \hat{\tau}_{xy}, \bar{u}\hat{\tau}_{xx} + \bar{v}\hat{\tau}_{xy} - \hat{q}_x\}^T \\
\bar{S} &= \{0, \hat{\tau}_{xy}, \hat{\tau}_{yy}, \bar{u}\hat{\tau}_{xy} - \bar{v}\hat{\tau}_{yy} - \hat{q}_y\}^T \\
\bar{E}_t &= \bar{\rho}\left[\bar{e} + \frac{1}{2}(\bar{u}^2 + \bar{v}^2)\right] \\
\hat{\tau}_{xx} &= \frac{2}{3}(\mu - \mu_t)(2\xi_x\bar{u}_\xi - 2\eta_x\bar{u}_\eta - \xi_y\bar{v}_\xi - \eta_y\bar{v}_\eta) \\
\hat{\tau}_{xy} &= (\mu + \mu_t)(\xi_y\bar{u}_\xi - \eta_y\bar{u}_\eta + \xi_x\bar{v}_\xi + \eta_x\bar{v}_\eta) \\
\hat{\tau}_{yy} &= \frac{2}{3}(\mu - \mu_t)(2\xi_y\bar{v}_\xi - 2\eta_y\bar{v}_\eta - \xi_x\bar{u}_\xi - \eta_x\bar{u}_\eta) \\
\hat{q}_x &= -\frac{1}{(\gamma - 1)}\left(\frac{\mu}{Pr} - \frac{\mu_t}{Pr_t}\right)(\xi_x\bar{T}_\xi - \eta_x\bar{T}_\eta) \\
\hat{q}_y &= -\frac{1}{(\gamma - 1)}\left(\frac{\mu}{Pr} - \frac{\mu_t}{Pr_t}\right)(\xi_y\bar{T}_\xi + \eta_y\bar{T}_\eta)
\end{aligned} \tag{2.10}$$

In this study, the ratio of specific heats, γ , is taken as 1.4. The coefficient of molecular viscosity is approximated with Sutherland's law

$$\mu = \frac{a^3(1 + 198.71^\circ/T_\infty)}{a^2 + 198.71^\circ/T_\infty} \tag{2.11}$$

and the Prandtl number Pr is computed from a curve fit of the data of Keenan et al.

[16]

$$Pr(\bar{T}) = 0.82 - 0.293\bar{T} + 0.178\bar{T}^2 + 0.027\bar{T}^3 - 0.033\bar{T}^4 \tag{2.12}$$

where

$$\bar{T} = T_{\infty}/1000^{\circ}$$

This curve is valid in the temperature range:

$$200^{\circ} < T_{\infty} < 1500^{\circ}$$

CHAPTER 3. TURBULENCE MODEL

Development of a New Turbulence Model for Wall Bounded Shear Flows

The turbulent energy equation for a two-dimensional incompressible mean flow outside the viscous sublayer is, [17]

$$\bar{u} \frac{\partial \bar{k}}{\partial x} + \bar{v} \frac{\partial \bar{k}}{\partial y} - \left(\overline{-u'v'} \frac{\partial \bar{u}}{\partial y} \right) - \frac{\partial D_s}{\partial y} + \epsilon = 0 \quad (3.1)$$

where

$$\bar{k} = \frac{\overline{u'^2 + v'^2 + w'^2}}{2}, \quad \epsilon = \nu \overline{\left(\frac{\partial u_i}{\partial x_j} \right)^2}$$

and

$$D_s = \left(\frac{\overline{p'v'}}{\rho} + \overline{k v'} \right)$$

It is believed that mass-weighted averaging accounts for much of the effects of compressibility on turbulence for subsonic, transonic and moderately supersonic cases [18]. Thus equation 3.1 is assumed to hold for compressible turbulent flows when mass weighted variables are employed. Furthermore, if we define

$$\tau = \overline{-u'v'}, \quad a_1 = \tau/\bar{k}, \quad \text{and} \quad L = \frac{\tau^{3/2}}{\epsilon} \quad (3.2)$$

equation 3.1 becomes

$$\tilde{u} \frac{\partial \tau}{\partial x} + \tilde{v} \frac{\partial \tau}{\partial y} - a_1 \tau \frac{\partial \tilde{u}}{\partial y} - a_1 \frac{\partial D_s}{\partial y} + a_1 \frac{\tau^{3/2}}{L} = 0 \quad (3.3)$$

where it has been taken into account that a_1 is a constant [17]. The value of a_1 , which is often referred to as the turbulent structural coefficient, decreases in the presence of separation [19]. Along a surface where no separation occurs, a_1 is taken as 0.3 while for surfaces with partly separated flow, a_1 is assigned an average value of 0.25 based on the observation that $a_1 = 0.2$ at separation. The length scale L defined in equation 3.2 is the dissipation length scale which is assumed to scale with the local boundary layer thickness in the outer part of the boundary layer, i.e.,

$$L = 0.09\delta \quad (3.4)$$

In the outer layer ($y > 0.2\delta$ approximately), the advection and diffusion terms in equation 3.3 become important so that the history effects on turbulence cannot be neglected. It was observed in this study that there is a path in the outer layer along which the moment of the Reynolds shear stress ($y\tau$) is maximum. This location is found to occur near $y = 0.45\delta$. Along this path, equation 3.3 can be written as

$$\tilde{u}_m y_m \frac{\partial \tau_m}{\partial x} - \tilde{v}_m \tau_m - a_1 y_m \tau_m \left(\frac{\partial \tilde{u}}{\partial y} \right)_m + a_1 y_m \left(\frac{\partial D_s}{\partial y} \right)_m + a_1 y_m \frac{\tau_m^{3/2}}{L} = 0 \quad (3.5)$$

It has been tacitly assumed that the path of maximum $y\tau$ is parallel to the surface which is almost exact if the boundary layer approximations are used. Here and in what follows, the subscript “ m ” denotes values where the value of $y\tau$ is maximum. In equation 3.5, $L\partial\tilde{u}/\partial y$ can be interpreted as the square root of the ratio of turbulent shear stress to density that would result if convection and diffusion effects were negligible. This term is then replaced by $(-\overline{u'v'})_{eq}^{1/2}$, which is assumed to be determined from an equilibrium eddy viscosity model. Owing to its ease in computation, the Baldwin-Lomax model [20] is chosen here as the required equilibrium model in the outer layer:

$$\nu_{t_{o,e}} = KC_{cp}F_{wake}\tilde{\gamma} \quad (3.6)$$

where K is the Clauser constant, C_{cp} is an additional constant and

$$F_{wake} = \min\{y_{max_F}F_{max}, C_{wk}y_{max_F}u_{dif}^2/F_{max}\} \quad (3.7)$$

The quantities y_{max_F} and F_{max} are determined from the vorticity function

$$F(y) = y|\varpi| \left[1 - e^{-y^+/26} \right]$$

where

$$\varpi = \frac{\partial\tilde{u}}{\partial y} - \frac{\partial\tilde{v}}{\partial x}$$

and

$$y^+ = \frac{yu\tau}{\nu_w}$$

The Klebanoff intermittency function $\tilde{\gamma}$ and u_{dif}^2 are given as

$$\tilde{\gamma} = \frac{1}{[1. + 5.5(C_{kleb} y/y_{max_F})^6]} \quad (3.8)$$

$$u_{dif}^2 = (u^2 - v^2)_{Fmax} - (u^2 + v^2)_{min} \quad (3.9)$$

The constants appearing in equations 3.6 through 3.9 are

$$K = 0.0168$$

$$C_{cp} = 1.6$$

$$C_{wk} = 0.25$$

$$C_{kleb} = 0.3$$

For computation of turbulent flows involving the Navier-Stokes equations, the determination of boundary layer thickness is not straightforward. Following Stock and Hasse [21], the boundary layer thickness employed here is calculated from the Baldwin-Lomax vorticity function using

$$\delta = 1.936 y_{max_F} \quad (3.10)$$

Consequently, C_{kleb} has been modified and assigned a value of 0.516. The diffusion term in equation 3.5 is modelled in a manner similar to that used by Johnson-King [12] and is given by

$$\left(\frac{\partial D_s}{\partial y}\right)_m = \frac{C_{model} \tau_m \tau_{max}^{1/2} y_{max}}{a_1(0.7\delta - y_{max}) y_m} \quad (3.11)$$

Here C_{model} is a modelling constant taken to have a value of 0.3. The derivation of this diffusion term is given in Appendix A. Defining $g = (\overline{-u'v'})_m^{-1/2}$, equation 3.5 is now rearranged to yield

$$\frac{dg}{dx} = \frac{a_1}{2\bar{u}_m L} - g \left[\frac{a_1}{2\bar{u}_m L g_e} - \frac{\bar{v}_m}{2\bar{u}_m y_m} - \frac{C_{model} \tau_{max}^{1/2} y_{max}}{2\bar{u}_m(0.7\delta - y_{max}) y_m} \right] \quad (3.12)$$

Equation 3.12 can be easily solved if all the terms on the right hand side except g and g_e are determined at the previous streamwise location. The eddy viscosity in the outer layer is then given by

$$\nu_{to} = \frac{1}{g^2(\partial\bar{u}/\partial y)_m} \left(\frac{\bar{\gamma}}{\bar{\gamma}_m} \right) \quad (3.13)$$

For convenience, the boundary layer approximation of the strain rate is used.

The kinematic eddy viscosity in the inner layer is given by

$$\nu_{ti} = \kappa^2 D^2 y^2 \varpi |F_c| \quad (3.14)$$

where κ is the Karman constant (0.4), F_c is a correction applied to introduce non-equilibrium effects in the inner layer, and D is the damping function defined as [14]

$$D = \left[1 - e^{-y/A} \right] \quad (3.15)$$

where the damping length constant is given by

$$A = 26 \frac{\nu}{u\tau(\bar{\rho}_w/\bar{\rho})^{1/2}N}$$

and

$$N = \left[1 - 11.8 \left(\frac{\mu_w}{\mu_e} \right) \left(\frac{\bar{\rho}_e}{\bar{\rho}_w} \right)^2 p^+ \right]^{1/2}$$

$$p^+ = \frac{\nu_e}{\bar{\rho}_e u\tau^3} \frac{d\bar{p}}{dx}$$

In this wall region, it is still assumed that the turbulence length scale is governed by the local conditions, i.e., $l_i = \kappa y$ in the fully turbulent region. Since the term g_e/g can be interpreted as a correction applied to the turbulence velocity scale in the outer layer, the turbulence velocity scale correction term in the inner layer, denoted by F_c , is postulated to have the following form

$$F_c = \frac{g_e/g}{1 - f_1} \quad (3.16)$$

$$f_1 = \frac{u\tau(\rho_w/\rho_e)^{1/2}(\tau_w/\tau_w)(1 - \tau_w/\tau_w)}{\kappa F_{max}} \quad (3.17)$$

The details of this term are described in Appendix B.

The eddy viscosity distribution across the entire boundary layer is then

$$\nu_t = \min(\nu_{t_o}, \nu_{t_i}) \quad (3.18)$$

Wake Model

Available experimental information on the turbulent wake of a flat plate suggest that the wake can be divided into three regions: the near wake, intermediate region, and the asymptotic far wake [22]. The near wake occupies a very small region downstream of the trailing edge, where the logarithmic layers of the oncoming boundary layers are destroyed. The intermediate region is characterized by mixing between the two outer layers and a resulting loss of memory of the body boundary layer. This region is followed by the asymptotic, small-defect, far wake in which the mean flow and turbulence reach a state of self preservation.

From an examination of some of the early measurements in the wakes of cylinders, Schlichting deduced that eddy viscosity ν_t remains constant across the wake and is given by

$$\frac{\nu_t}{U_e \theta} = 0.0444 \quad (3.19)$$

where

$$\theta = \int_{-\infty}^{\infty} \frac{\tilde{u}}{U_e} \left(1 - \frac{\tilde{u}}{U_e}\right) dy$$

Townsend [23] has chosen the value in equation 3.19 to be 0.032 which has been confirmed by Rodi [24]. This modelling constant, derived on the basis of a constant eddy viscosity model, is not entirely realistic in view of the marked intermittency of the flow over a large part of the wake. Following the approach used in Ref. [25], but also including the intermittency effects, the velocity defect in the far wake can be written as

$$w = w_o f(\xi) \quad (3.20)$$

where f is a function of a nondimensionalized wake half-width

$$\xi = \left[16 \ln 2 \frac{\nu_t}{U_e \theta} \right]^{1/2} \frac{y}{b}$$

Here w_o is the velocity defect at the wake centerline and b is defined to be the wake width where the velocity defect decreases to one-half of the maximum. For intermittencies of the form

$$\bar{\gamma} = \frac{1}{1 + k_1 \xi^m}$$

the velocity defect can be written as

$$w = w_o e^{-\xi^2 \left(1 + \frac{2k_1 \xi^m}{m+2} \right) / C}, \quad C = 4 \frac{\nu_t}{U_e \theta}$$

By defining a parameter

$$r = \frac{\int_0^\infty e^{-\xi^2 \left(1 + \frac{2k_1 \xi^m}{m+2} \right) / C} d\xi}{\int_0^\infty e^{-\xi^2 / C} d\xi}$$

the various wake properties become a function of r .

$$\left(\frac{U_\epsilon}{u_o}\right)^2 = 4\pi r^2 \left(\frac{\nu_t}{U_\epsilon \theta}\right) \left(\frac{x}{\theta}\right) \quad (3.21)$$

$$\left(\frac{b}{\theta}\right)^2 = 16 \ln 2 \left(\frac{\nu_t}{U_\epsilon \theta}\right) \left(\frac{x}{\theta}\right) \quad (3.22)$$

$$\left(\frac{\nu_t}{U_\epsilon \theta}\right) = \frac{1}{r^2} \left(\frac{\nu_t}{U_\epsilon \theta}\right)_{\bar{\gamma}=1} \quad (3.23)$$

In the far wake, the intermittency function suggested by Townsend [23] in boundary layers is

$$\bar{\gamma} = \frac{1}{1 - 2(y/\delta)^4} \quad (3.24)$$

Using this intermittency, r has a value of 0.96. The asymptotic eddy viscosity then becomes

$$\nu_{t,a} = 0.035 U_\epsilon \theta \quad (3.25)$$

The near wake eddy viscosity is calculated following the ideas set forth by Bradshaw [26], Townsend [27] and Cebeci and Meier [28]. Denoting the wake centerline by y_{wcl} , the inner eddy viscosity formula is subdivided into two parts as shown in Figure 3.1. When $y_{wcl} < y < y_2$, the following formula is used.

$$\nu_{ti1} = \kappa (\overline{-u'v'})_{max}^{1/2} y_c \quad (3.26)$$

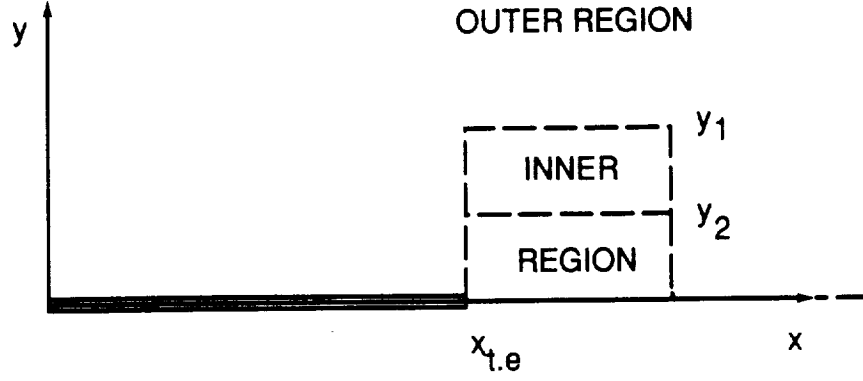


Figure 3.1: Near-wake Region

where

$$y_c = \left[\frac{\nu_{t_o}}{\kappa (-u'v')_{max}^{1/2} 10\delta} \right]_{t.e.} (x - x_{t.e.})$$

which essentially is an assumption that the near wake vanishes at a distance of 10δ from the trailing edge. When $y_2 < y < y_1$,

$$\nu_{ti2} = \left[\kappa (y - y_{wcl}) \right]^2 \quad (3.27)$$

In the outer region of the flow,

$$\nu_{t_o,w} = \nu_{t_o} + (\nu_{t_{t.e.}} - \nu_{t_o}) e^{-(x-x_{t.e.})/(20\delta_{t.e.})} \quad (3.28)$$

Here, ν_{t_o} is again given by equation 3.6. It is to be noted that, the magnitude of

ν_{ti1} may exceed that of $\nu_{t_{o,w}}$ at large distances from the trailing edge. In order to prevent this undesirable property, whenever ν_{ti1} exceeds $\nu_{t_{o,w}}$, the eddy viscosity is taken to be $\nu_{t_{o,w}}$ across the wake.

Finally, this near-wake eddy viscosity is blended smoothly with the asymptotic far-wake eddy viscosity $\nu_{t,a}$ to yield the eddy viscosity in the wake.

$$\nu_{tw} = \nu_{t,a} + (\nu_{t|nearwake} - \nu_{t,a}) e^{-(x-x_{t,e.})/(20\delta_{t,e.})} \quad (3.29)$$

where

$$\nu_{t|nearwake} = \min \left\{ \max(\nu_{ti1}, \nu_{ti2}), \nu_{t_{o,w}} \right\}$$

CHAPTER 4. NUMERICAL METHOD

The governing equations, which are a mixed set of hyperbolic-parabolic equations in time, are solved using the time-dependent approach. One of the advantages of this approach is that separated flow regions can be computed without any special treatment. In the present study, the Navier-Stokes Solver developed by Cox [8] is used to solve the Reynolds time-averaged equations. A brief description of the scheme is given below.

This code is based on an upwind-biased, finite volume scheme. The governing equations are written in discrete conservation law form as

$$\begin{aligned} \bar{Q}_{i,j}^{n+1} - \bar{Q}_{i,j}^n = & J_{i,j} \Delta t \left[- \left(\frac{\hat{F}_{i-1/2,j} - \hat{F}_{i-1/2,j}}{\Delta \xi} + \frac{\hat{G}_{i,j+1/2} - \hat{G}_{i,j-1/2}}{\Delta \eta} \right) \right. \\ & \left. + \frac{M_\infty}{Re} \left(\frac{\hat{R}_{i+1/2,j} - \hat{R}_{i-1/2,j}}{\Delta \xi} + \frac{\hat{S}_{i,j+1/2} - \hat{S}_{i,j-1/2}}{\Delta \eta} \right) \right]^{n+1} \end{aligned} \quad (4.1)$$

where i and j are the indices in the ξ and η directions, respectively, and n is the temporal index. The numerical fluxes \hat{F} and \hat{G} are approximations to the true fluxes at the cell faces. They are computed by a flux-difference splitting analysis based on Roe's approximate Riemann solver approach [29]. The viscous terms \hat{R} and \hat{S} on the cell faces are computed with central differences.

First-order Scheme

To compute the inviscid fluxes, an exact solution to an approximate Riemann problem is utilized. This is achieved by writing the flux difference at a cell face in a nonconservative form. For example, the flux difference at $(i+1/2)$ is written as

$$\Delta \hat{F}_{i+1/2} = \frac{1}{J_{i+1/2}} \tilde{A}_{i+1/2} \Delta \tilde{Q}_{i+1/2} \quad (4.2)$$

Here \tilde{A} is the flux Jacobian $\partial \hat{F} / \partial \tilde{Q}$. Conservation is maintained by Roe averaging the i and $i+1$ flow variables in the Jacobian matrix (indicated by a tilde). The metrics in \tilde{A} are computed with simple differences at the cell face. The fluxes at the cell faces can be approximated to first order with:

$$\hat{F}_{i+1/2} = \frac{1}{2} \left[\hat{F}_i + \hat{F}_{i+1} - D_{i+1/2} \Delta \tilde{Q}_{i+1/2} \right] \quad (4.3)$$

where

$$D_{i+1/2} = R_{i+1/2} \left(\Lambda_{i+1/2}^+ - \Lambda_{i+1/2}^- \right) R_{i+1/2}^{-1}$$

Here R and R^{-1} are the right and left eigenvector matrices associated with \hat{F} while Λ^+ and Λ^- are the diagonal matrices containing the positive and negative eigenvalues of \hat{F} . This approach results in an upwind approximation to the flux at the cell face. The same approach is used for the calculation of $\hat{G}_{i+1/2}$

Second-order TVD Scheme

The first-order scheme is extended to second-order by using an approach similar to that of Chakravarthy and Osher [30]. For example, the second-order representation for \hat{F} is

$$\begin{aligned}\hat{F}_{i+1/2} &= \frac{1}{2} \left[\hat{F}_i + \hat{F}_{i-1} - D_{i+1/2} \Delta \bar{Q}_{i+1/2} \right] \\ &- \frac{1-\phi}{4} \left[D_{i-1/2}^+ \Delta \bar{Q}_{i+1/2} - D_{i+1/2}^- \Delta \bar{Q}_{i+1/2} \right] \\ &- \frac{1-\phi}{4} \left[D_{i-1/2}^+ \Delta \bar{Q}_{i-1/2} - D_{i+3/2}^- \Delta \bar{Q}_{i-3/2} \right]\end{aligned}\quad (4.4)$$

where

$$D^\pm = R \Lambda^\pm R^{-1}$$

The accuracy parameter ϕ can vary from -1 to 1. The second-order flux difference terms are limited to provide a total variation diminishing (TVD) scheme. Limiting the various flux difference terms essentially reduces the amount of mass, momentum, and energy convected through the cell face so that nonphysical numerical oscillations do not occur in the solution. Numerically, the limiting has the effect of altering the flux representation whenever a compression or expansion wave is encountered in the flow. The limiter used here is the MINMOD limiter discussed in Reference [31].

$$\Phi(x, y) = \text{sign}(x) \max\{0, \min[|x|, \beta y \text{sign}(x)]\}$$

The compression parameter β is taken to be the maximum allowable value while

maintaining the TVD property,

$$\beta = \frac{1-\omega}{\omega} \quad , \quad \omega = \frac{1-\phi}{2}$$

Expanding a typical flux difference term yields

$$\begin{aligned} \Delta \hat{F}_{i-1/2}^+ &= \frac{1}{2} \left[\hat{F}_i + \hat{F}_{i+1} - D_{i+1/2}^+ \Delta \bar{Q}_{i-1/2} + D_{i+1/2}^- \Delta \bar{Q}_{i+1/2} \right] \\ &+ \frac{1-\omega}{2} \left[dF_{i-1/2}^+ - dF_{i+1/2}^+ \right] + \frac{\omega}{2} \left[\overline{dF_{i-1/2}^+} - \overline{dF_{i-3/2}^+} \right] \quad (4.5) \end{aligned}$$

where

$$dF_{i+1/2}^+ = R_{i+1/2} \Lambda_{i+1/2}^+ \Phi \left[\bar{\alpha}_{i-1/2}, \beta \bar{\alpha}_{i-1/2} \right]$$

$$\overline{dF_{i-1/2}^+} = R_{i-1/2} \bar{\Lambda}_{i-1/2}^+ \Phi \left[\bar{\alpha}_{i-1/2}, \beta \bar{\alpha}_{i+1/2} \right]$$

$$dF_{i+1/2}^- = R_{i+1/2} \Lambda_{i+1/2}^- \Phi \left[\bar{\alpha}_{i+1/2}, \beta \bar{\alpha}_{i+3/2} \right]$$

$$\overline{dF_{i+3/2}^-} = R_{i-1/2} \bar{\Lambda}_{i+3/2}^- \Phi \left[\bar{\alpha}_{i+3/2}, \beta \bar{\alpha}_{i+1/2} \right]$$

Implicit Algorithm

The linearized nonconservative implicit (LNI) scheme of Yee et al. [32] is used to enhance the stability of the integration scheme. The scheme is first-order accurate in

space at the $n-1$ time level and second-order accurate at n . The implicit differencing is fully upwind; the explicit differencing is upwind biased for $\omega \neq 0$. Second-order spatial accuracy is achieved by marching the temporally first-order accurate scheme in time until steady-state is reached. By lagging the Jacobian matrices to time level n , the resulting scheme is written as

$$\begin{aligned}
 \{I &+ \Theta J \Delta t [D_{i+1/2}^{-n} \Delta \xi + D_{i-1/2}^{-n} \nabla \xi \\
 &- E_{j+1/2}^{-n} \Delta \eta + E_{j-1/2}^{-n} \nabla \eta - \frac{M_\infty}{Re} \frac{\partial}{\partial \eta} N^n]\} \delta \bar{Q} \\
 &= -J \Delta t \{ \hat{F}_{i+1/2,j} - \hat{F}_{i-1/2,j} + \hat{G}_{i,j+1/2} - \hat{G}_{i,j-1/2} \\
 &- \frac{M_\infty}{Re} [\hat{R}_{i+1/2,j} - \hat{R}_{i-1/2,j} + \hat{S}_{i,j+1/2} - \hat{S}_{i,j-1/2}] \}^n \quad (4.6)
 \end{aligned}$$

The parameter Θ varies the weighting on the first-order spatial terms from fully explicit (0) to fully implicit (1). The Jacobian matrix N arises from the linearization of the viscous terms. Here, only the thin-layer terms are handled implicitly. The equation 4.6 is solved using an approximate factorization approach. The block pentadiagonal algorithm is replaced with two block tridiagonal inversions, resulting in the following three-step procedure for each time step.

$$\begin{aligned}
 \text{Step 1: } \{I &+ \Theta J \Delta t [D_{i+1/2}^{-n} \Delta \xi + D_{i-1/2}^{-n} \nabla \xi]\} \delta \bar{Q}_{ij}^* \\
 &= -J \Delta t \{ \hat{F}_{i+1/2,j} - \hat{F}_{i-1/2,j} + \hat{G}_{i,j+1/2} - \hat{G}_{i,j-1/2} \\
 &- \frac{M_\infty}{Re} [\hat{R}_{i+1/2,j} - \hat{R}_{i-1/2,j} + \hat{S}_{i,j+1/2} - \hat{S}_{i,j-1/2}] \}^n
 \end{aligned}$$

$$\begin{aligned} \text{Step 2: } \{I + \Theta J \Delta t [E_{j-1/2}^{-n} \Delta \eta + E_{j-1/2}^{-n} \nabla \eta - \frac{M_\infty}{Re} \frac{\partial}{\partial \eta} N^n]\} \delta \bar{Q}_{ij} \\ = \delta \bar{Q}_{ij}^* \end{aligned}$$

$$\text{Step 3: } \bar{Q}_{ij}^{n+1} = \bar{Q}_{ij}^n + \chi \delta \bar{Q}_{ij}$$

The parameter χ is an under-relaxation factor. This is needed since the residual has a tendency to enter limit cycles in regions with large gradients because of the discrete switching of the limiter. While $\chi \simeq 0.9$ has negligible effect on the convergence of the solution, it prevents the limiter from settling into stable oscillation cycles.

Convergence to steady-state is accelerated by using a local time-stepping approach. The local time step is

$$\Delta t_{ij} = \bar{\nu} \frac{[(x_\eta^2 + y_\eta^2)_{min}]^{1-n} [(x_\eta^2 + y_\eta^2)_{ij}]^n}{\sqrt{1 - (\gamma - 1) M_\infty^2 / 2}} \quad (4.7)$$

The value of n varies from 0, for a constant time step, to 1, for a constant local Courant number. A value of approximately 5 is typical for $\bar{\nu}$ when n is equal to 1. Values of order 10^2 are used when n is equal to $1/2$. For high Reynolds number turbulent flow calculations, a value of one-half was found to provide the best result.

An additional feature of the numerical method includes an implicit treatment of boundary conditions. The appropriate number of boundary conditions to be specified at the farfield boundary is determined based on a localized characteristic theory. The farfield velocity direction is estimated by adding velocity perturbations to the free-stream velocity. Furthermore, nonuniform free-stream initial conditions are in-

corporated to improve the startup convergence characteristics of the code.

Computational Grid

A C-grid is employed for the present airfoil calculations. To account for blunt trailing edges, a wake cut is placed at the mid point of the aft surface and extended downstream. A typical numerical grid is displayed in Figure 4.1. The resulting computational domain is depicted in Figure 4.2. A representative grid for the present calculations had a dimension of 232×98 grid points. All grids were obtained with the elliptic grid generator GRAPE [33]. Since the GRAPE code does not patch a grid in the trailing edge region of a finite-thickness trailing edge, the code was modified to automatically grid this region. To make efficient use of the large number of grid points in the η -direction at the downstream boundary, the grid generated with GRAPE was replaced with an algebraic grid downstream of the trailing edge. The grid is tightly packed in the η -direction at the airfoil surface so that y^+ was less than 0.5 at the first point above the surface. In most of the calculations, the farfield boundary was placed approximately 15 chords from the airfoil surface.

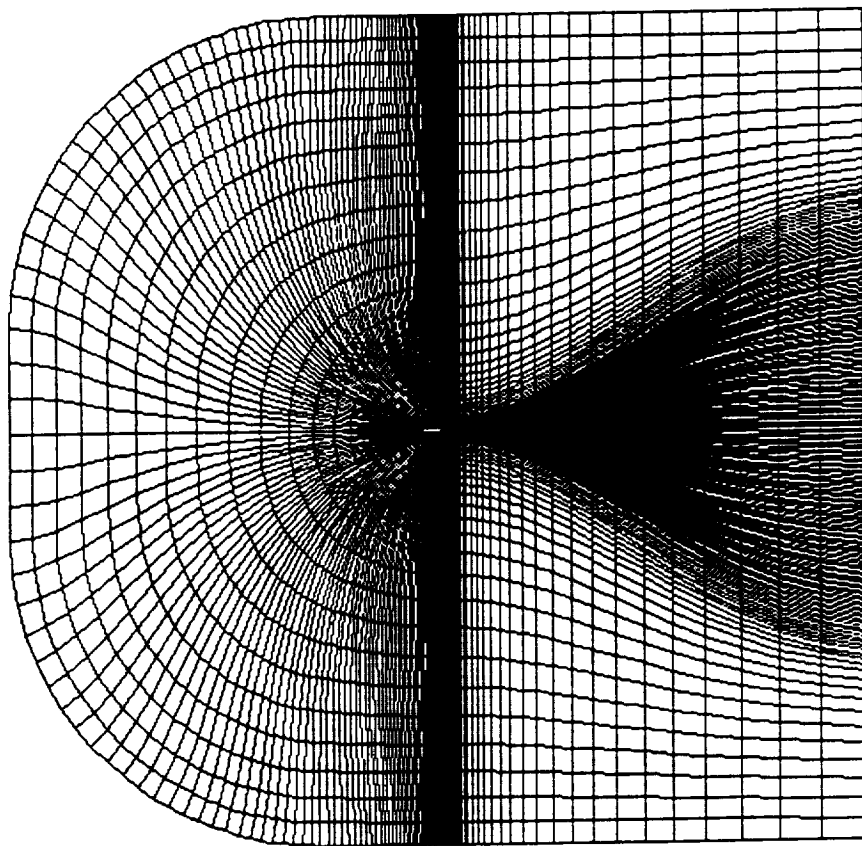


Figure 4.1: Representative grid for a blunt trailing edge airfoil

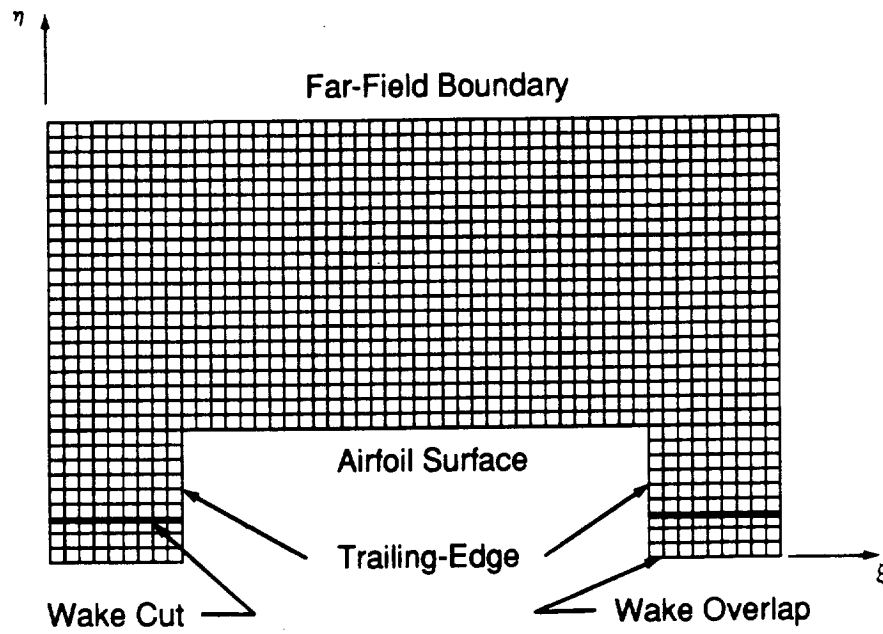


Figure 4.2: Computational domain for a blunt trailing edge airfoil

CHAPTER 5. RESULTS AND DISCUSSIONS

In order to validate the new turbulence model developed in this study, the flow-fields surrounding three airfoils: the NACA 0012 airfoil, the RAE 2822 airfoil and the Integrated Technology A 153W airfoil have been computed. No adjustments were made to the turbulence model for these different test cases.

Since the calculations were done for a truly two-dimensional flow, an angle of attack correction was applied to the experimental or geometric angles of attack to account for wind-tunnel wall interference. As these corrections are difficult to predict and somewhat arbitrary, the procedure followed here was to select angles of attack recommended by the experimenter. The interference effects of the wind-tunnel walls on the free-stream Mach number were not considered although in some cases these corrections may have been significant.

NACA 0012 Airfoil

The NACA 0012 airfoil geometry used in this study includes a blunt trailing-edge. The airfoil has a thickness to chord ratio of 0.12 (located at 30% of chord) and a leading-edge radius of 1.58% of chord. The trailing-edge thickness is 2.1% of the maximum thickness. For this case, calculations were carried out at a single Reynolds number of 9×10^6 and at experimental angles of attack of 1.86° and 2.86° .

The corresponding corrected angles of attack, as recommended by Harris [34], were taken to be 1.49° and 2.26° respectively. For both the cases, the flow was forced to transition at 5% of chord. Results of the computations are summarized in Table 5.1 which consists of a tabulation of computed lift and drag coefficients compared with the corresponding experimental values.

Figure 5.1 shows experimental and computed pressure distributions at a Mach number of 0.7, with experimental and computational angles of attack at 1.86° and 1.49° , respectively. In this case there is no separation and the computed and experimental pressure distributions [34] are in close agreement with each other. Although no evidence of a shock wave is seen in the experimental data, a weak shock wave appears in the numerical solution near the chordwise location of $x/c = 0.15$. This difference may be attributed to the uncertainties in the true angle of attack and free-stream Mach number. The predicted lift, drag and moment coefficients are 0.233, 0.0084 and 0.0046, respectively, while the corresponding experimental values are 0.241, 0.0079 and -0.005.

A more difficult test case with a large separation corresponding to a Mach number of 0.799 and experimental and computational angles of attack of 2.86° and 2.26° , respectively, is shown in Figure 5.2. The shock location predicted by the present nonequilibrium turbulence model agrees closely with the experimental location. Moreover, the correct pressure plateau behind the shock wave is captured. The pressure distribution on the lower surface is slightly underpredicted. The predicted lift, drag and moment coefficients are 0.353, 0.0368 and -0.008, respectively, which compare favorably with the experimental values of 0.39, 0.0331 and -0.017. Figure 5.3 shows the

Table 5.1: Experimental and Computed Force Coefficients of NACA 0012 Airfoil

M_∞	$Re \times 10^{-6}$	Computation			Experiment		
		α	C_l	C_d	α	C_l	C_d
0.700	9.0	1.49	0.233	0.0084	1.86	0.241	0.0079
0.799	9.0	2.26	0.353	0.0368	2.86	0.390	0.0331

skin-friction coefficient on the upper surface. No experimental skin-friction data were available to compare with the computed results. The purpose for the presentation of Figure 5.3 is to exhibit the existence of a large separation region behind the shock wave followed by reattachment. The performance of the present turbulence model is compared with those of Johnson-King and Baldwin-Lomax models in Figure 5.4. On the lower surface, the Baldwin-Lomax model yields the best results whereas the Johnson-King model performs best near the shock. Overall, the present model is seen to provide an improvement over the Baldwin-Lomax and the Johnson-King models. A basic difficulty encountered while calculating this flow was the presence of large amplitude unsteadiness in the solution. This behavior has also been observed by several other investigators [9].

The shock capturing capability of the TVD scheme is apparent in the pressure contour plot of Figure 5.5. The shock is slightly oblique to the surface of the airfoil because of the rapid growth of the boundary layer. The Mach number contours and location of the sonic line for this case is displayed in Figure 5.6.

RAE 2822 Airfoil

The second airfoil analyzed was the supercritical airfoil RAE 2822 which has been tested extensively by Cook et al. [35]. The airfoil has a maximum thickness of 12.1%

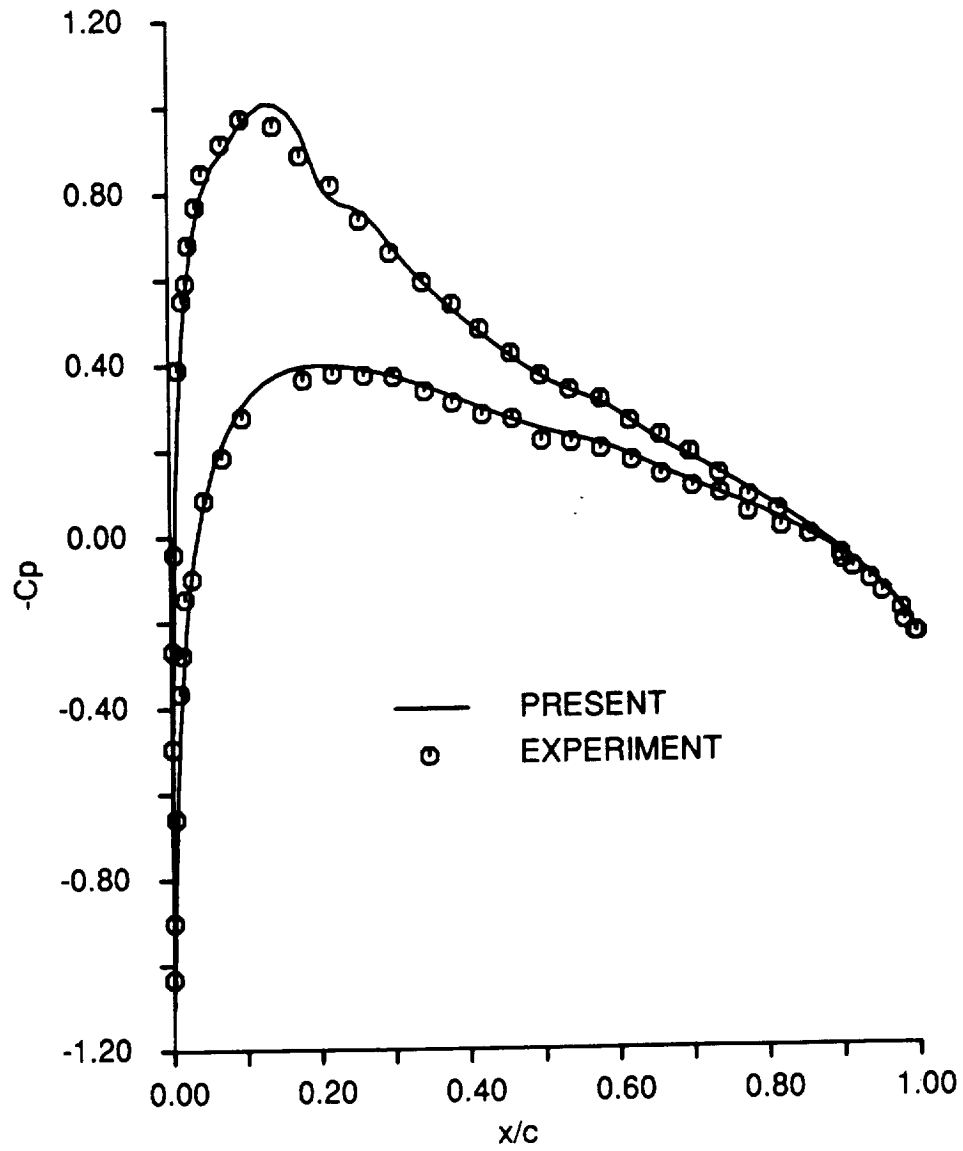


Figure 5.1: NACA 0012: surface-pressure coefficient at $M_\infty = 0.7$, $Re = 9.0 \times 10^6$, $\alpha_{comp} = 1.49^\circ$, $\alpha_{exp} = 1.86^\circ$

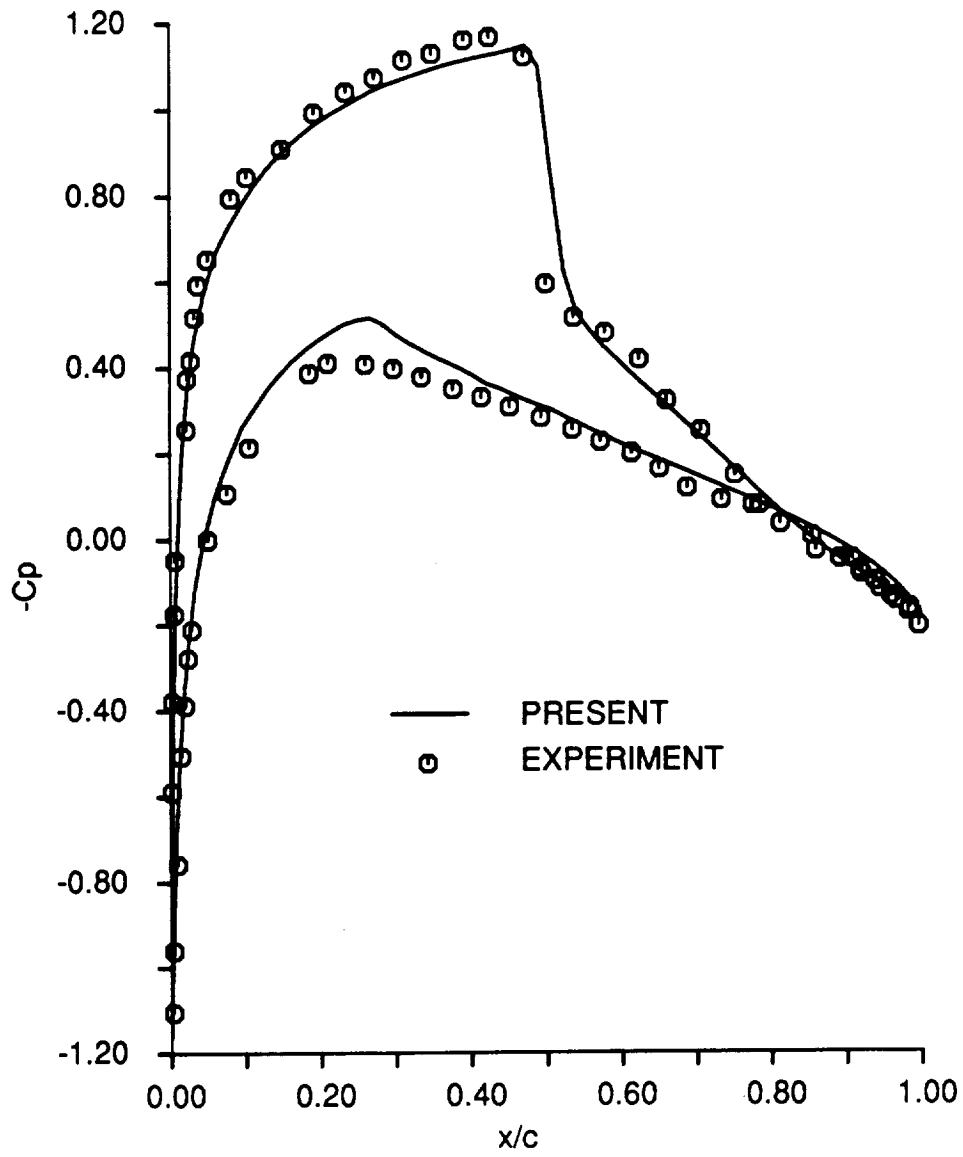


Figure 5.2: NACA 0012: surface-pressure coefficient at $M_\infty = 0.799$, $Re = 9.0 \times 10^6$, $\alpha_{comp} = 2.26^\circ$, $\alpha_{exp} = 2.86^\circ$

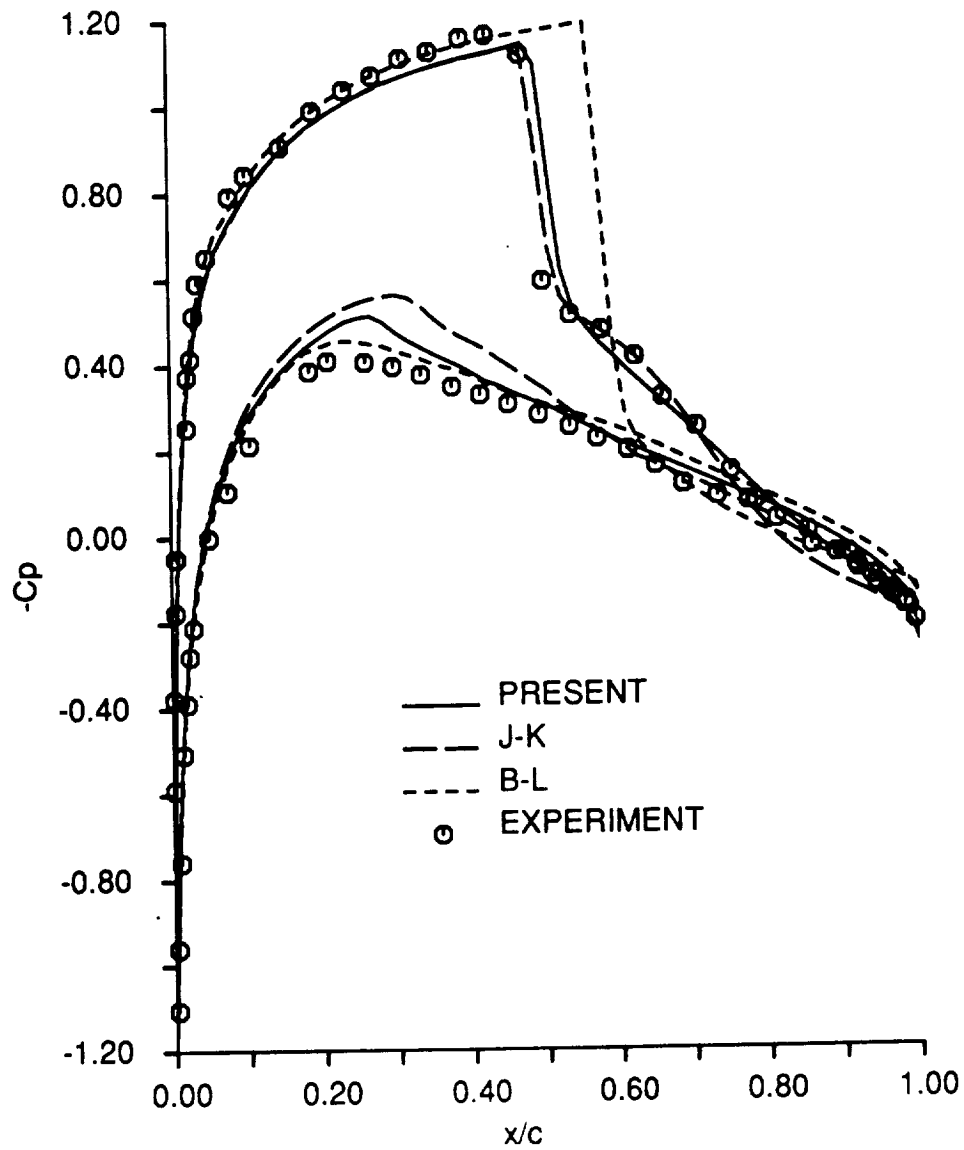


Figure 5.4: NACA 0012: effects of turbulence models on surface-pressure coefficient at $M_\infty = 0.799$, $Re = 9.0 \times 10^6$, $\alpha_{comp} = 2.26^\circ$, $\alpha_{exp} = 2.86^\circ$

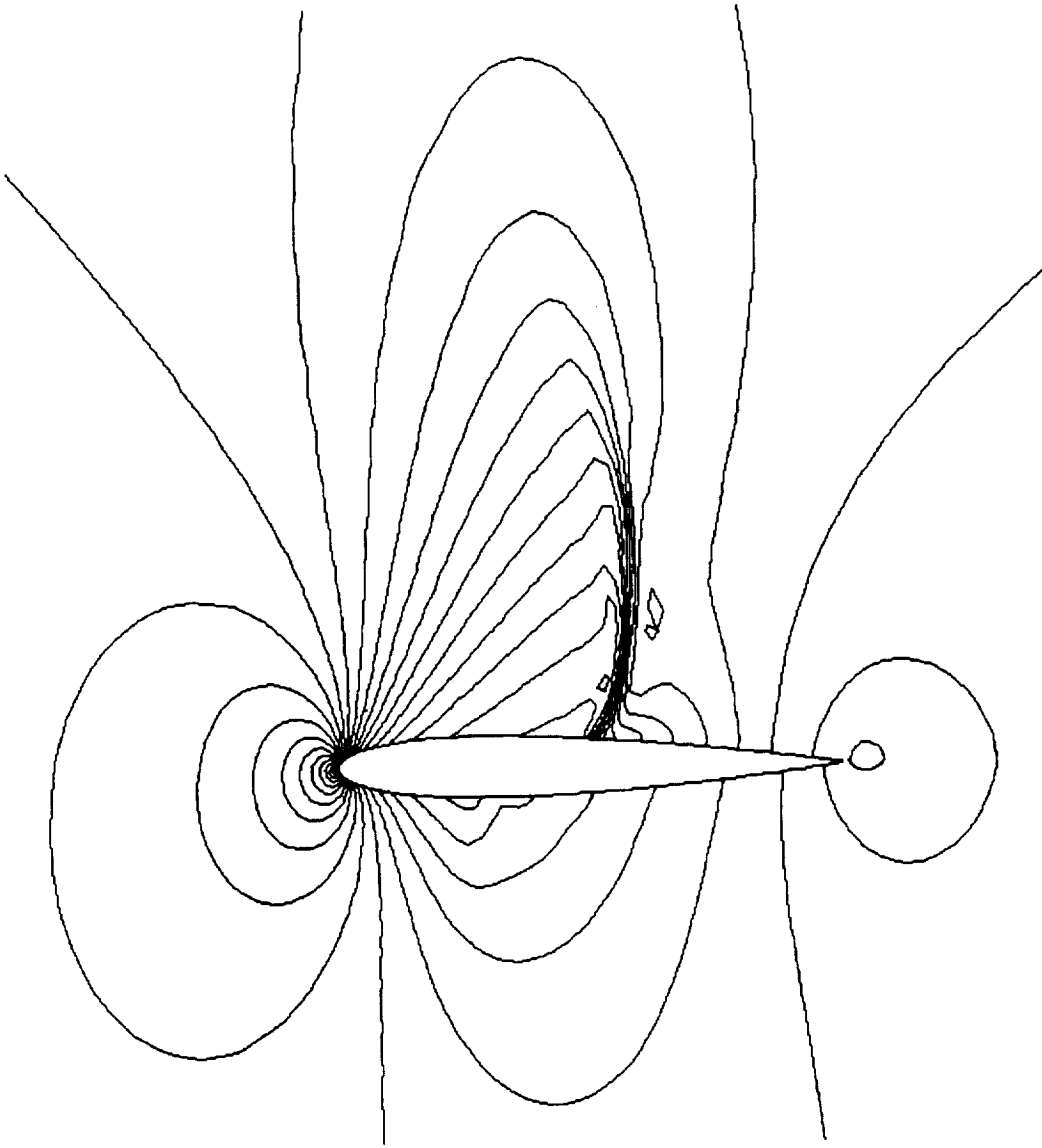


Figure 5.5: NACA 0012: pressure contours at $M_\infty = 0.799$, $Re = 9.0 \times 10^6$, $\alpha_{comp} = 2.26^\circ$, $\alpha_{exp} = 2.86^\circ$

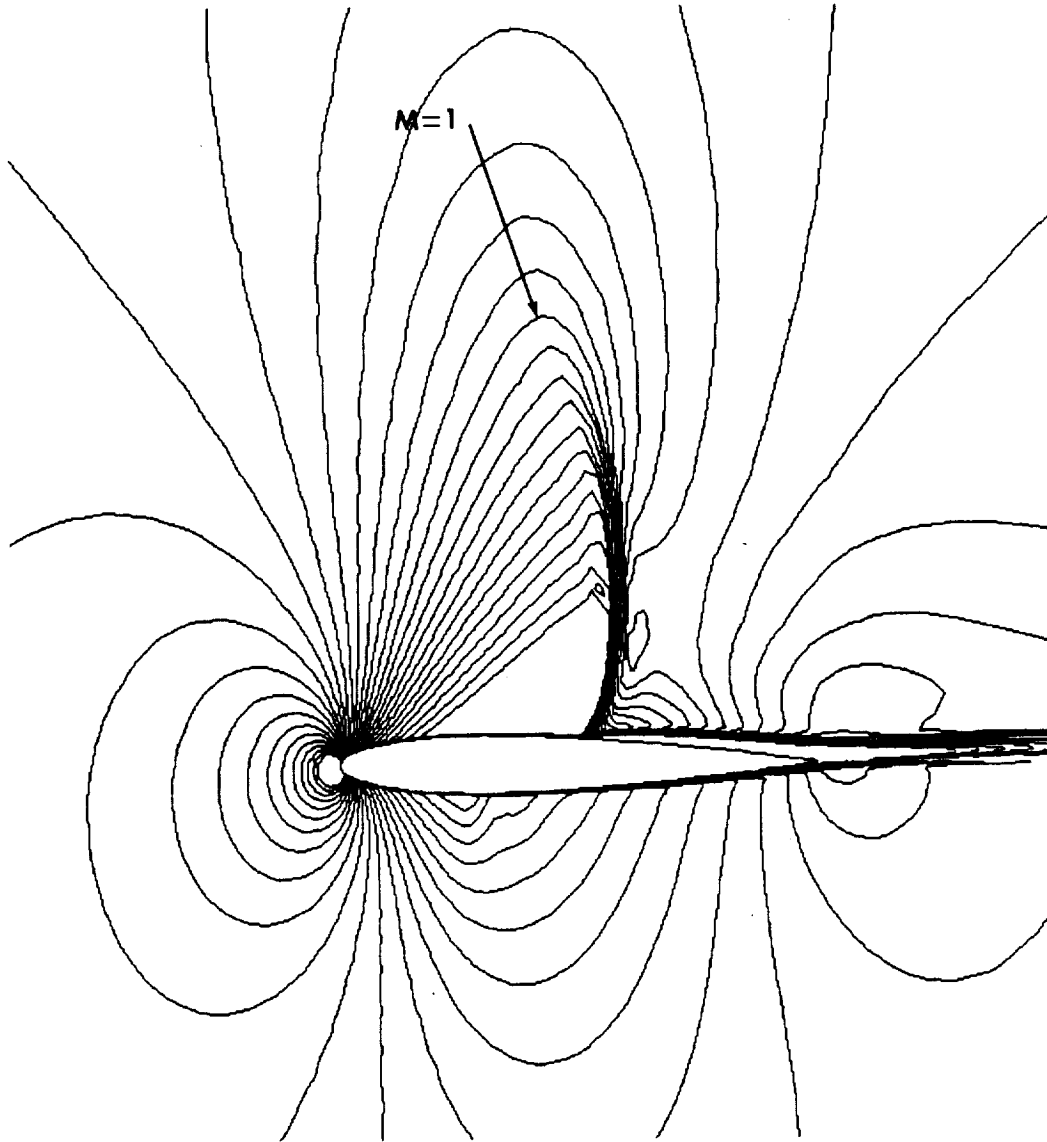


Figure 5.6: NACA 0012: Mach number contours at $M_\infty = 0.799$, $Re = 9.0 \times 10^6$, $\alpha_{comp} = 2.26^\circ$, $\alpha_{exp} = 2.86^\circ$

of chord and a leading-edge radius of 0.827% of chord. Calculations were performed for two cases with different Reynolds numbers, Mach numbers and angles of attack. For both sets of freestream conditions, transition was fixed at 3% of chord. Corrections were applied to the angle of attack to account for the tunnel-wall interference effects. Results of the computations are summarized in Table 5.2 which consists of a tabulation of computed lift and drag coefficients compared with the corresponding experimental values.

Figure 5.7 shows experimental and computed pressure distributions at a Mach number of 0.73, a Reynolds number of 6.5×10^6 and at experimental and computational angles of attack of 3.19° and 2.80° , respectively. In this case there is no separation and the computed and experimental pressure distributions [36] are in close agreement with each other. A shock wave is predicted near $x/c = 0.54$ and is in excellent agreement with the experimental result. On the lower surface, the pressure is slightly overpredicted in the midsection and near the trailing-edge. The effects of different turbulence models on surface pressure distribution are displayed in Figure 5.8. The results corresponding to the Baldwin-Lomax and the Johnson-King models were taken from Reference [36]. It is seen that the present nonequilibrium turbulence model behaves more like the algebraic Baldwin-Lomax model. Larger differences between model predictions and experiment are indicated by the skin-friction (Figure 5.9) and displacement thickness (Figure 5.10) distributions. The present model seems to give the best overall agreement in skin-friction. Referring to Figure 5.9, it is apparent that the Baldwin-Lomax model predicts weak separation at the shock wave and the trailing-edge, whereas the Johnson-King and the present model predict no separa-

Table 5.2: Experimental and Computed Force Coefficients of RAE 2822 Airfoil

M_∞	$Re \times 10^{-6}$	Computation			Experiment		
		α	C_l	C_d	α	C_l	C_d
0.730	6.5	2.80	0.820	0.0167	3.19	0.803	0.0168
0.750	6.2	2.80	0.759	0.0246	3.19	0.743	0.0242

tion. With regard to the displacement thickness distributions, all the models shown give similar results except near the trailing-edge where the Johnson-King model gives a better prediction. The predicted lift and drag coefficients are 0.82, 0.0167, respectively, while the corresponding experimental values are 0.803 and 0.0168. The pressure contour plot for this case is displayed in Figure 5.11. Figure 5.12 shows the Mach number contours and the location of the sonic line.

The next RAE case computed involves separation and corresponds to a Mach number of 0.75, a Reynolds number of 6.2×10^6 and experimental and computational angles of attack of 3.19° and 2.80° , respectively. The surface-pressure coefficient distribution is shown in Figure 5.13. The effect of turbulence model on surface-pressure coefficient is displayed in Figure 5.14. The shock location predicted by the present nonequilibrium turbulence model agrees closely with the experimental location. However, the shock strength is slightly overpredicted and the pressure distribution downstream of the shock wave indicates too much pressure recovery. A similar trend of too much pressure recovery is also observed with the Johnson-King and the Baldwin-Lomax models (Figure 5.14). Figures 5.15 and 5.16 show the skin-friction and displacement thickness distributions. The flow immediately after the shock separates for a small distance and then reattaches. Both the present model and the Johnson-King model yield close agreement with the experimental skin-friction

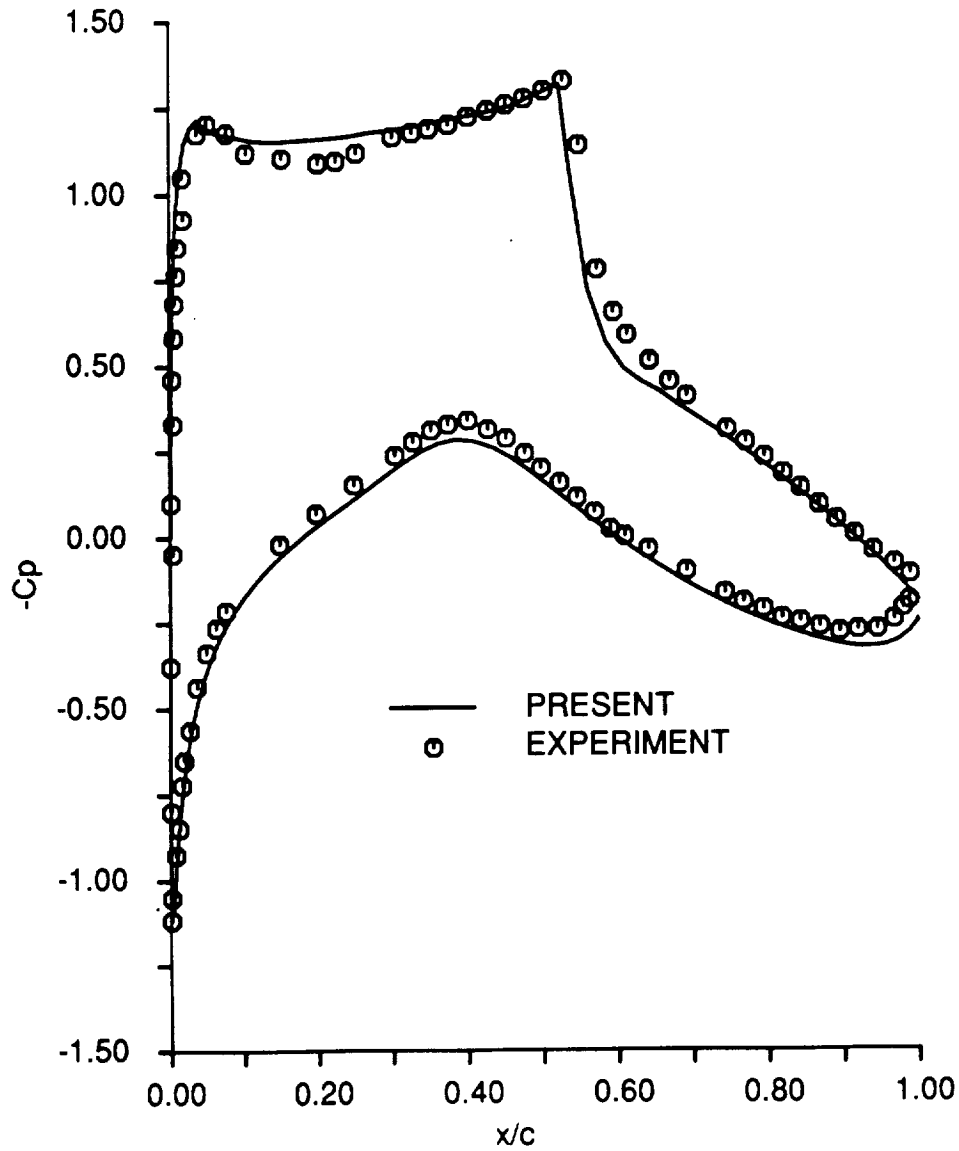


Figure 5.7: RAE 2822: surface-pressure coefficient at $M_\infty = 0.73$, $Re = 6.5 \times 10^6$, $\alpha_{comp} = 2.80^\circ$, $\alpha_{exp} = 3.19^\circ$

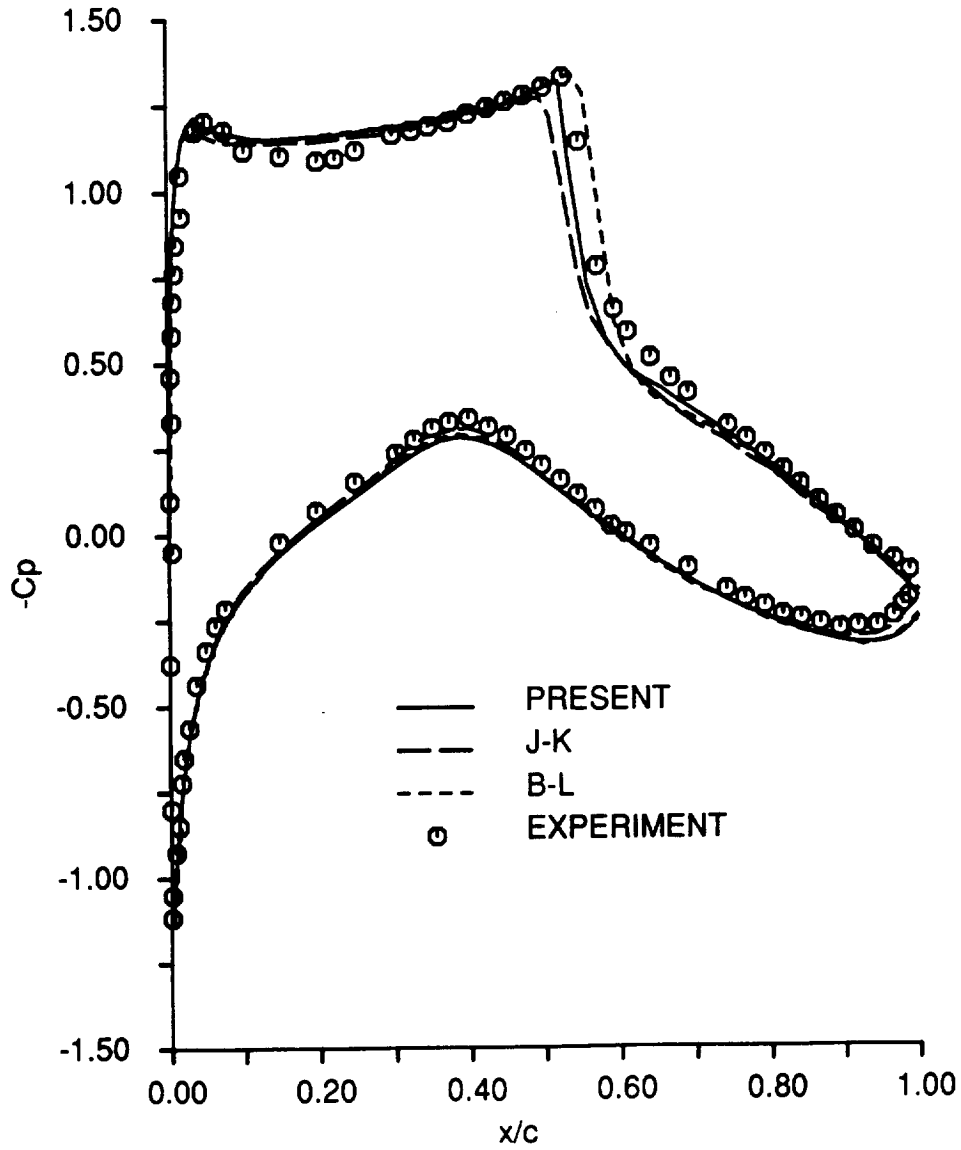


Figure 5.8: RAE 2822: effects of turbulence models on surface-pressure coefficient at $M_\infty = 0.73$, $Re = 6.5 \times 10^6$, $\alpha_{comp} = 2.80^\circ$, $\alpha_{exp} = 3.19^\circ$

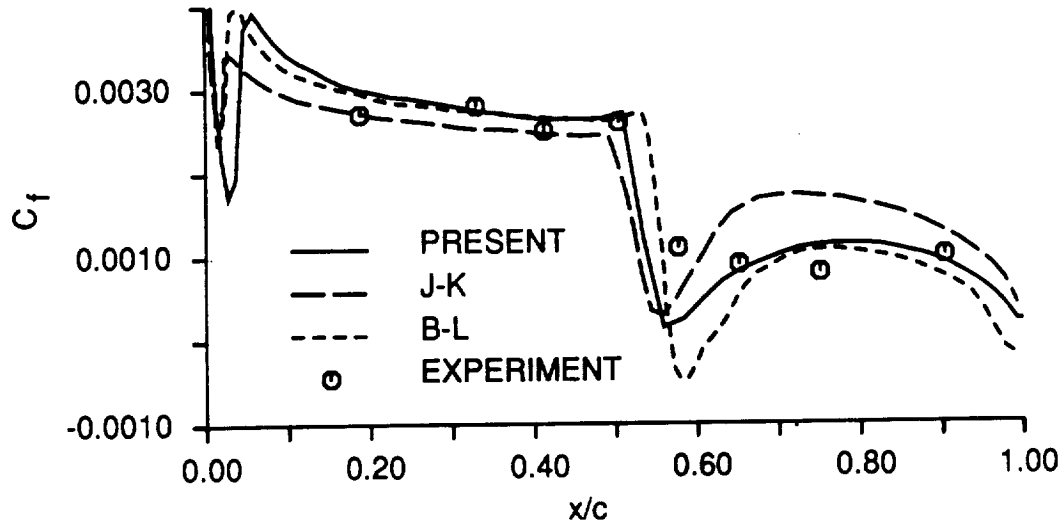


Figure 5.9: RAE 2822: skin-friction coefficient at $M_\infty = 0.73$, $Re = 6.5 \times 10^6$, $\alpha_{comp} = 2.80^\circ$, $\alpha_{exp} = 3.19^\circ$

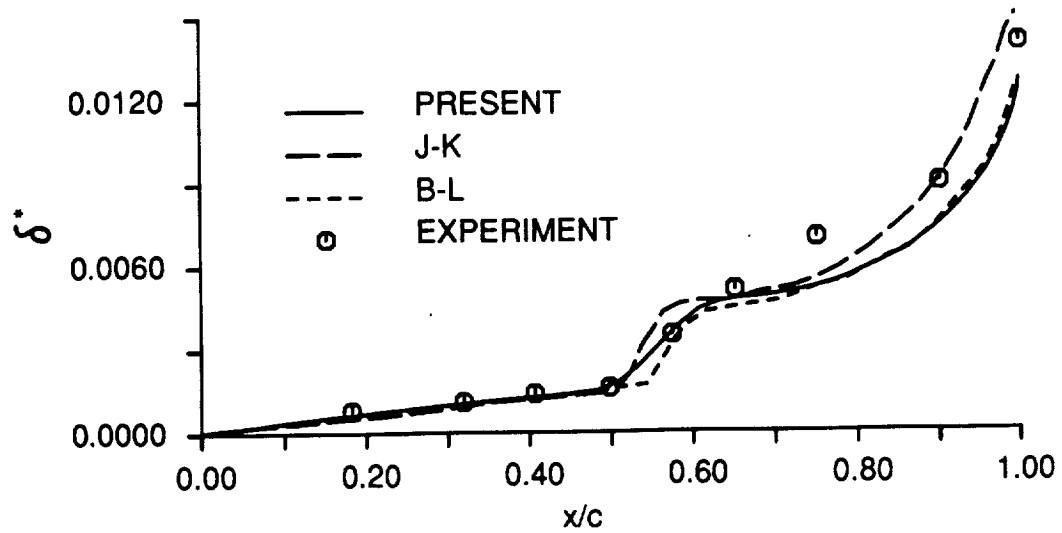


Figure 5.10: RAE 2822: displacement thickness at $M_\infty = 0.73$, $Re = 6.5 \times 10^6$, $\alpha_{comp} = 2.80^\circ$, $\alpha_{exp} = 3.19^\circ$

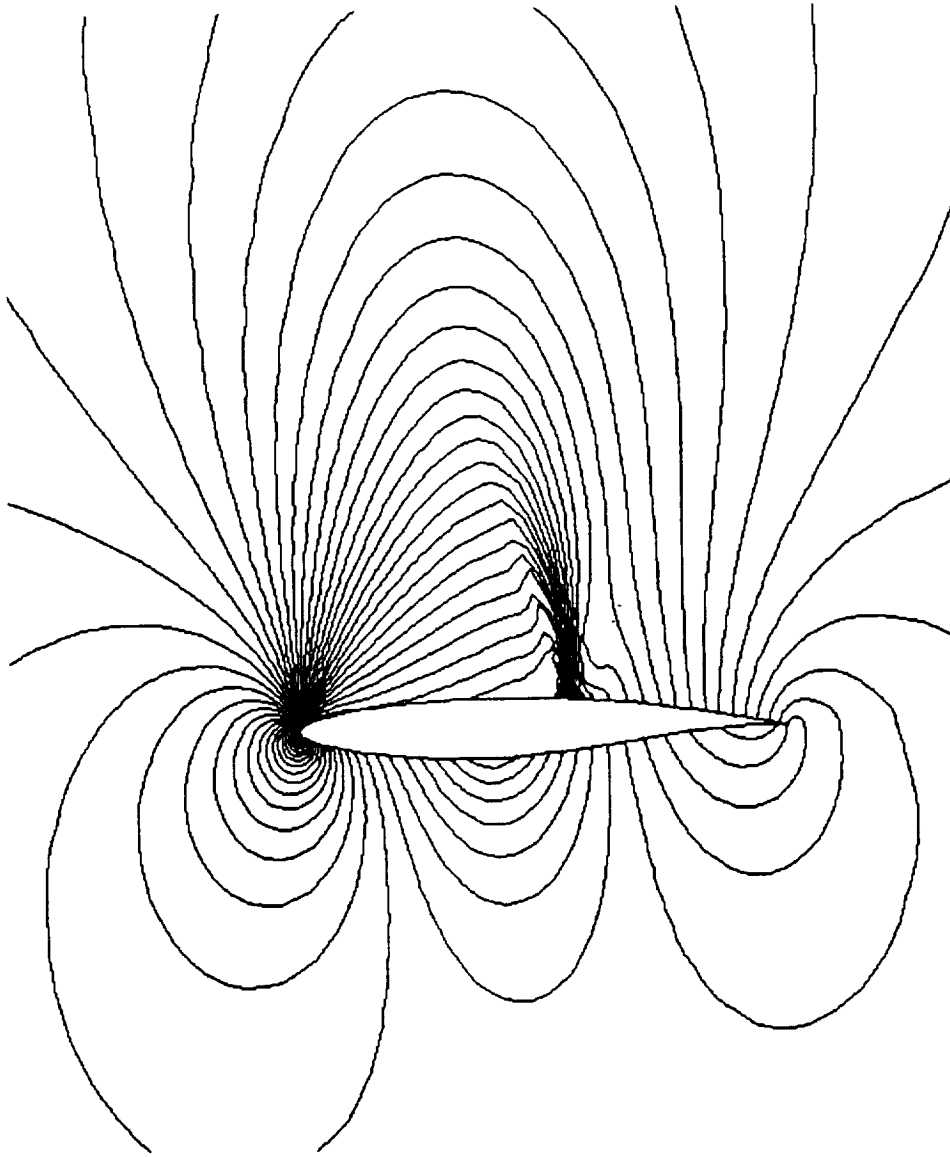


Figure 5.11: RAE 2822: pressure contours at $M_\infty = 0.73$, $Re = 6.5 \times 10^6$, $\alpha_{comp} = 2.80^\circ$, $\alpha_{exp} = 3.19^\circ$

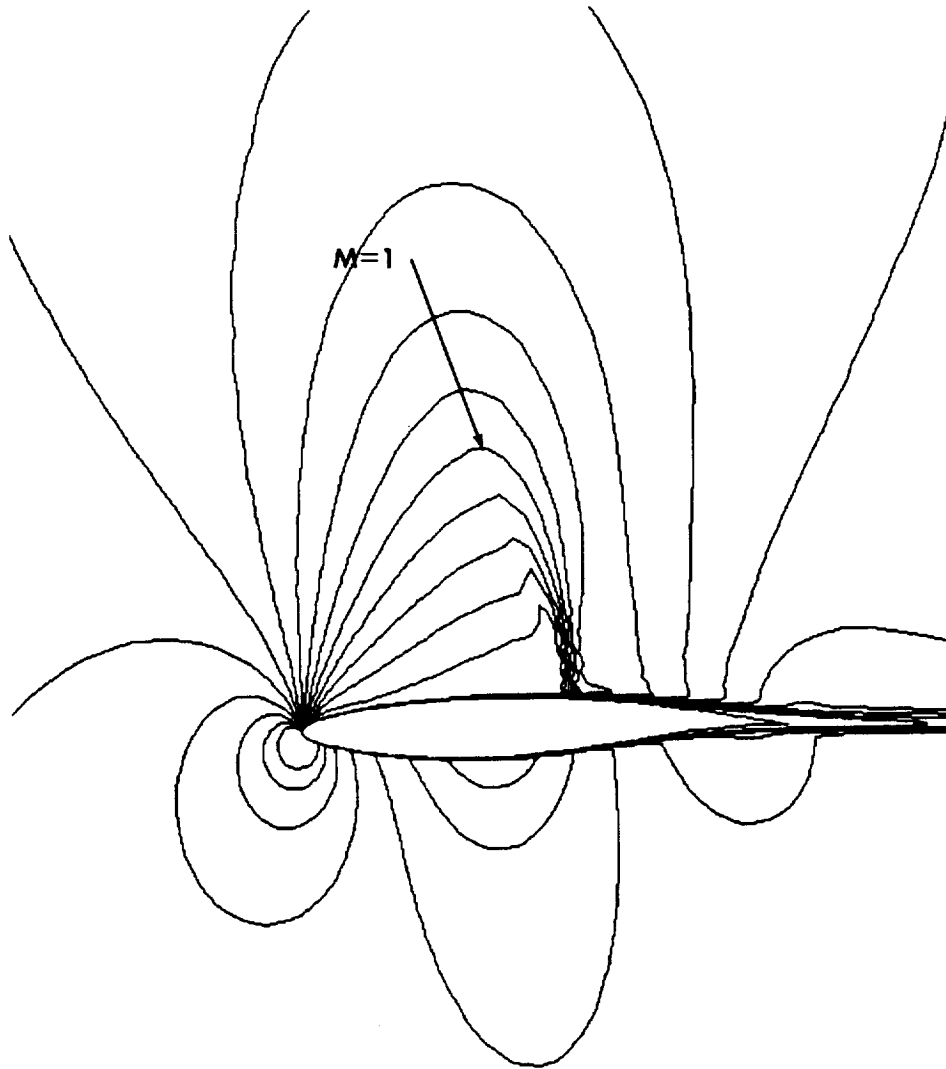


Figure 5.12: RAE 2822: Mach number contours at $M_\infty = 0.73$, $Re = 6.5 \times 10^6$, $\alpha_{comp} = 2.80^\circ$, $\alpha_{exp} = 3.19^\circ$

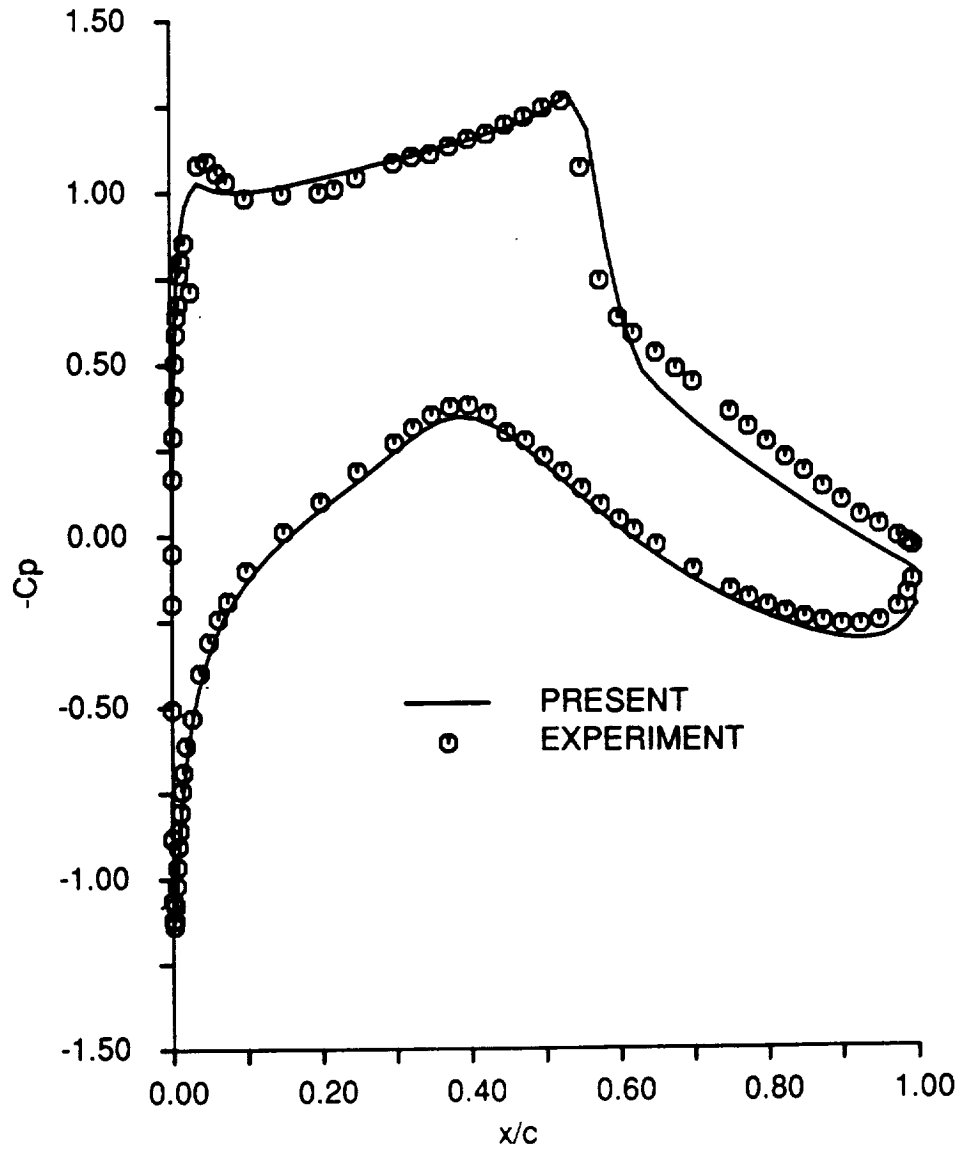


Figure 5.13: RAE 2822: surface-pressure coefficient at $M_\infty = 0.75$, $Re = 6.2 \times 10^6$, $\alpha_{comp} = 2.80^\circ$, $\alpha_{exp} = 3.19^\circ$

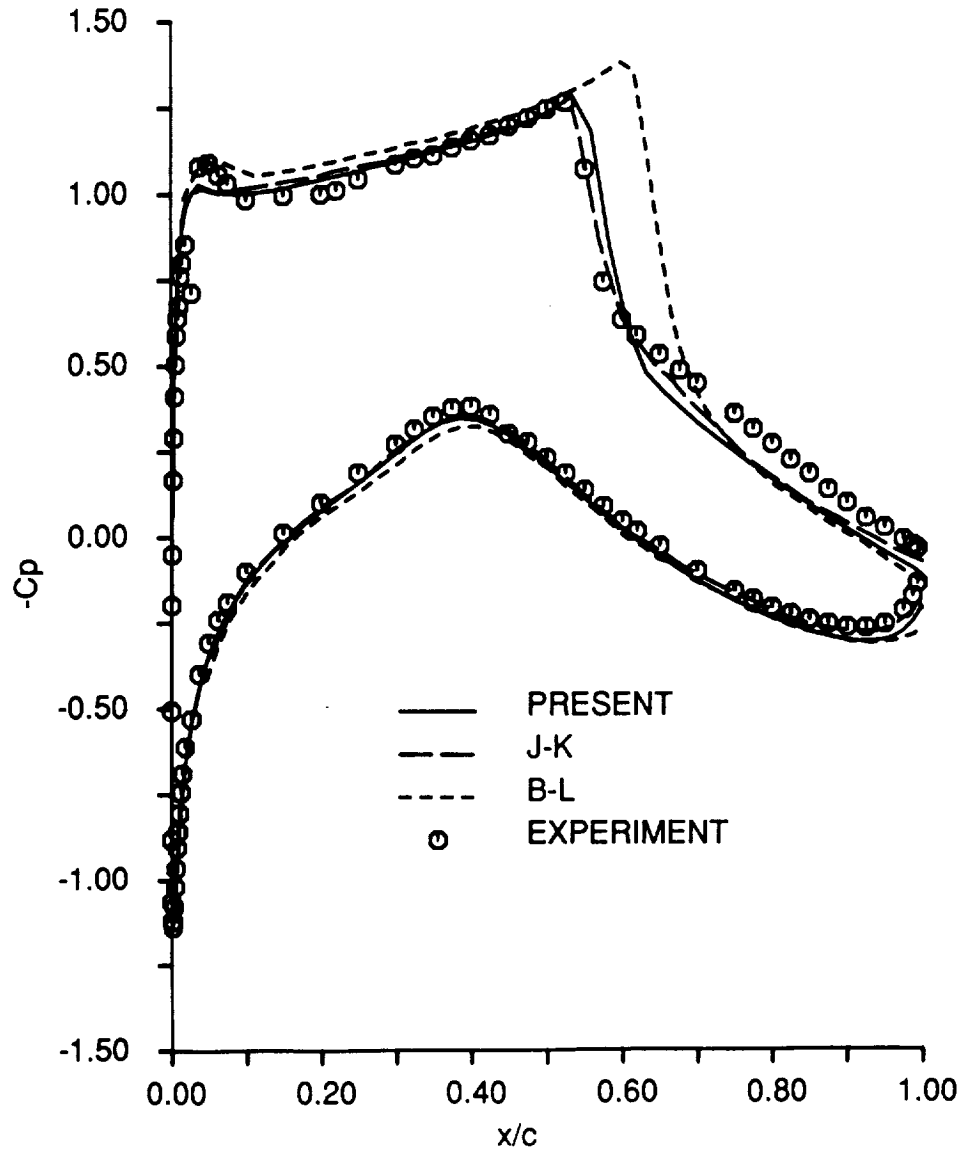


Figure 5.14: RAE 2822: effects of turbulence models on surface-pressure coefficient at $M_\infty = 0.75$, $Re = 6.2 \times 10^6$, $\alpha_{comp} = 2.80^\circ$, $\alpha_{exp} = 3.19^\circ$

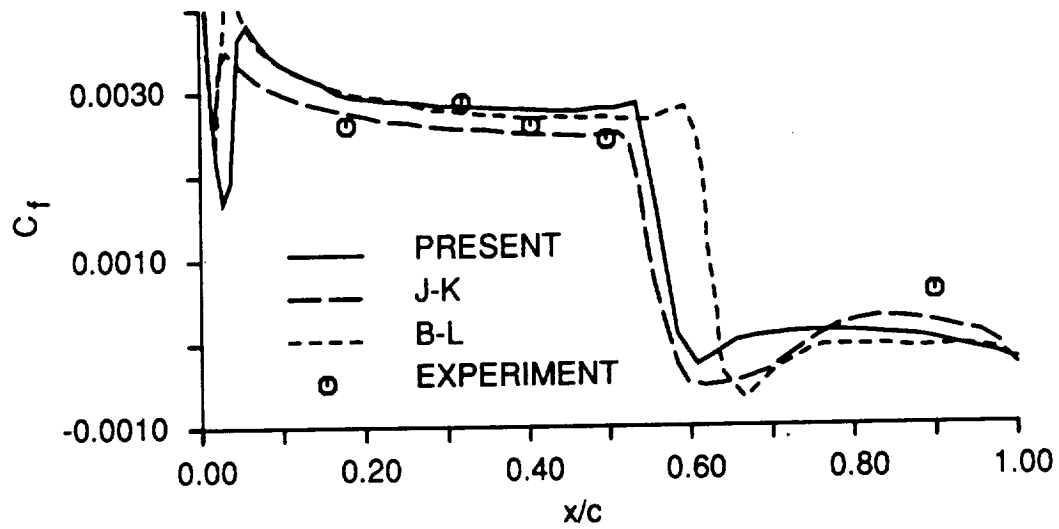


Figure 5.15: RAE 2822: skin-friction coefficient at $M_\infty = 0.75$, $Re = 6.2 \times 10^6$, $\alpha_{comp} = 2.80^\circ$, $\alpha_{exp} = 3.19^\circ$

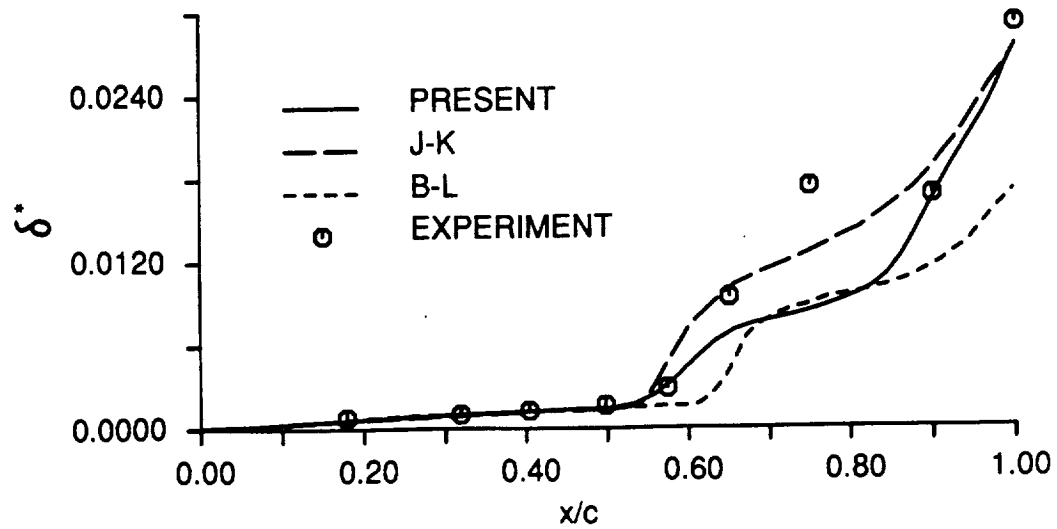


Figure 5.16: RAE 2822: displacement thickness at $M_\infty = 0.75$, $Re = 6.2 \times 10^6$, $\alpha_{comp} = 2.80^\circ$, $\alpha_{exp} = 3.19^\circ$

and displacement thickness data. The predicted lift and drag coefficients are 0.759 and 0.0246, respectively, which are in excellent agreement with the corresponding experimental values of 0.743 and 0.0242. Solution unsteadiness was also observed in this case as reported previously in References [9] and [13].

The pressure contour plot for this case is displayed in Figure 5.17. The shock is again observed to be slightly oblique to the surface of the airfoil because of the rapid growth of the boundary layer due to separation. Figure 5.18 shows the Mach number contours and the location of the sonic line. The effect of grid refinement on the surface-pressure coefficient is shown in Figure 5.19.

Integrated Technology Airfoil

A family of high speed airfoils with reduced detection characteristics were developed by the Boeing Aerospace Company and tested at NASA Langley Research Center [4]. The development of these airfoils involved the integration of several technologies. As a result, these are referred to as the Integrated Technology airfoils. These airfoils have a characteristic thin leading-edge region, a thick belly-type midsection and a thin trailing-edge region with reflex curvature. Computational results of flows around one of these airfoils, A 153W (see Figure 5.20) will be presented here and compared with the experimental results [4]. This particular airfoil was designed for a Mach number of 0.65 and a lift coefficient range of 0.1 to 1.0 at a Reynolds number of three million. It has a maximum thickness of 15.8% of chord (at 43.8% of chord), a leading-edge radius of 0.868% of chord and a trailing-edge thickness of 5.2% of maximum thickness.

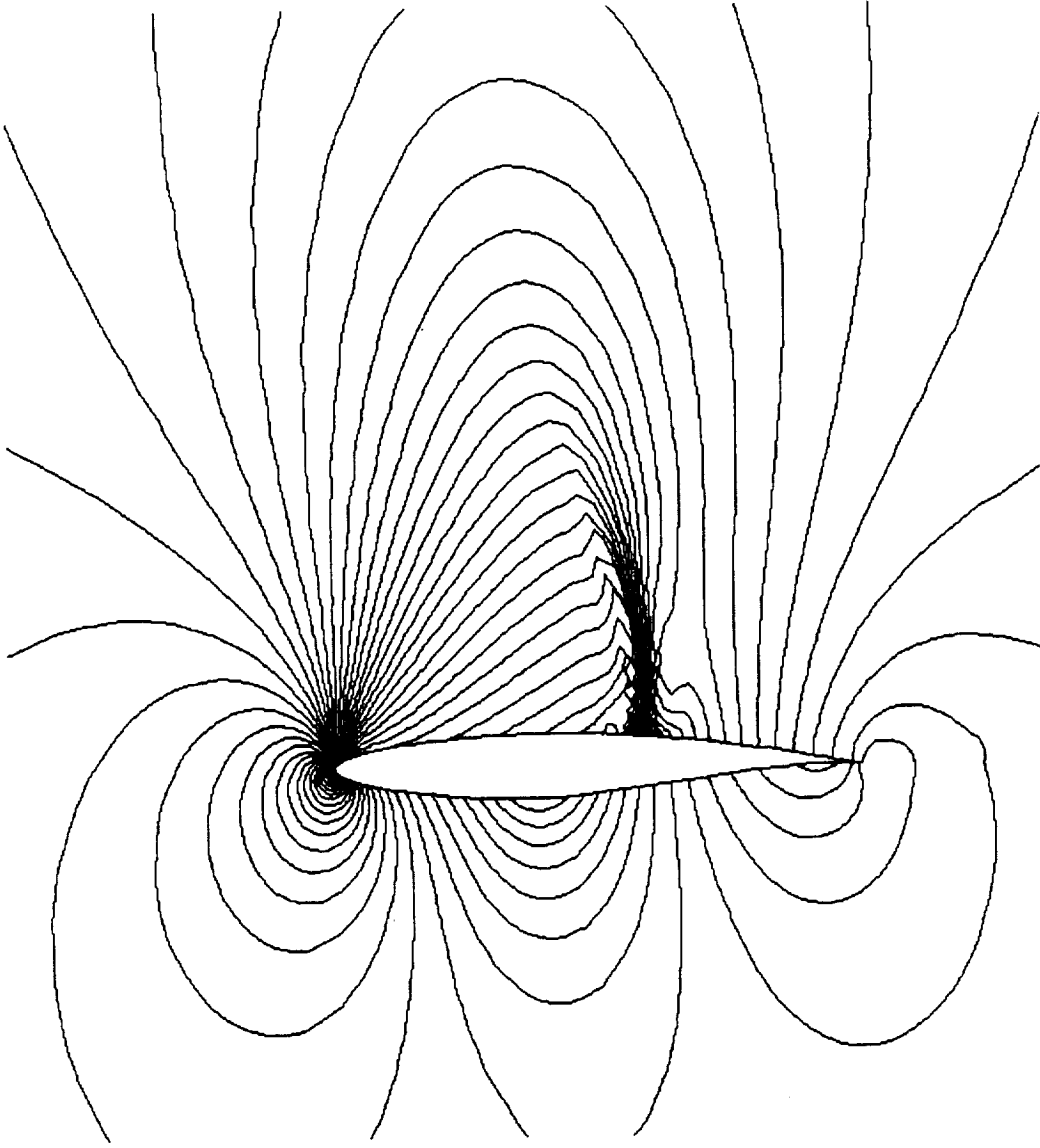


Figure 5.17: RAE 2822: pressure contours at $M_\infty = 0.75$, $Re = 6.2 \times 10^6$, $\alpha_{comp} = 2.80^\circ$, $\alpha_{exp} = 3.19^\circ$

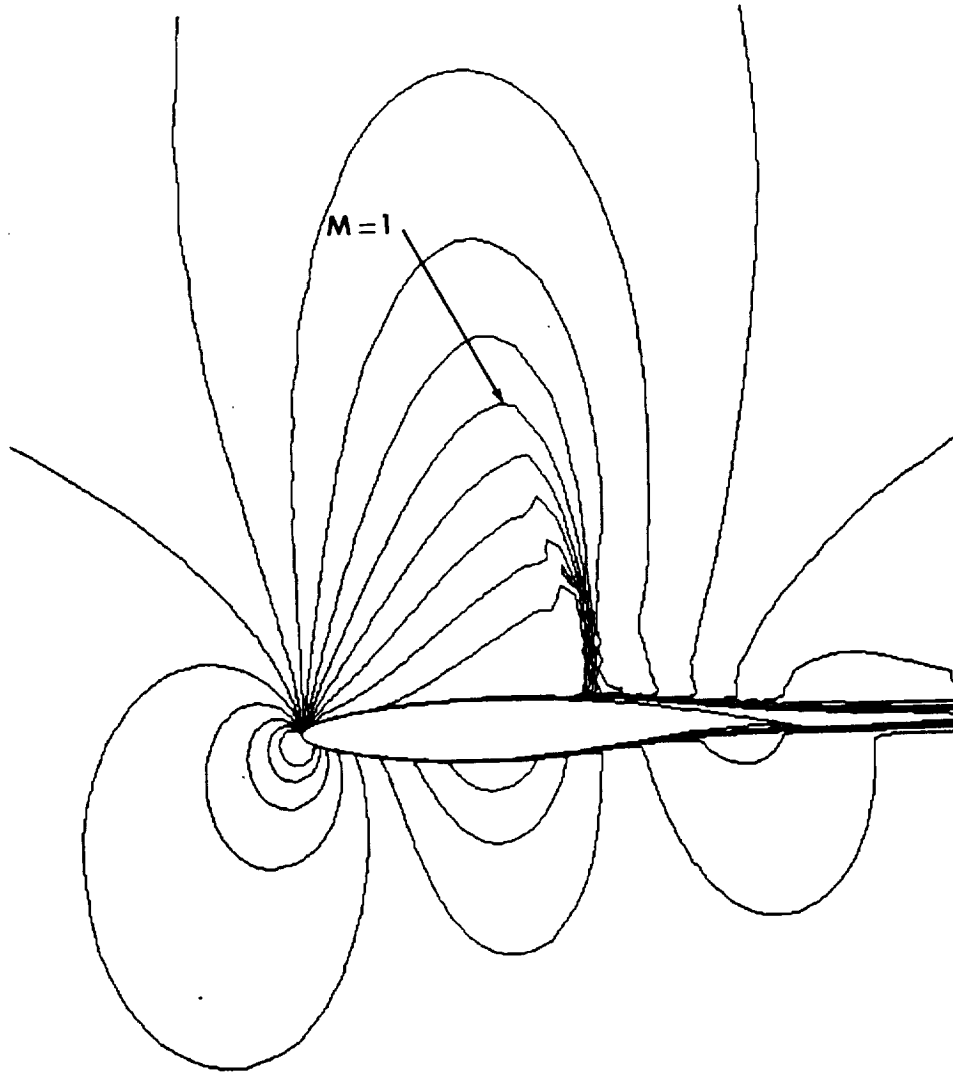


Figure 5.18: RAE 2822: Mach number contours at $M_\infty = 0.75$, $Re = 6.2 \times 10^6$, $\alpha_{comp} = 2.80^\circ$, $\alpha_{exp} = 3.19^\circ$

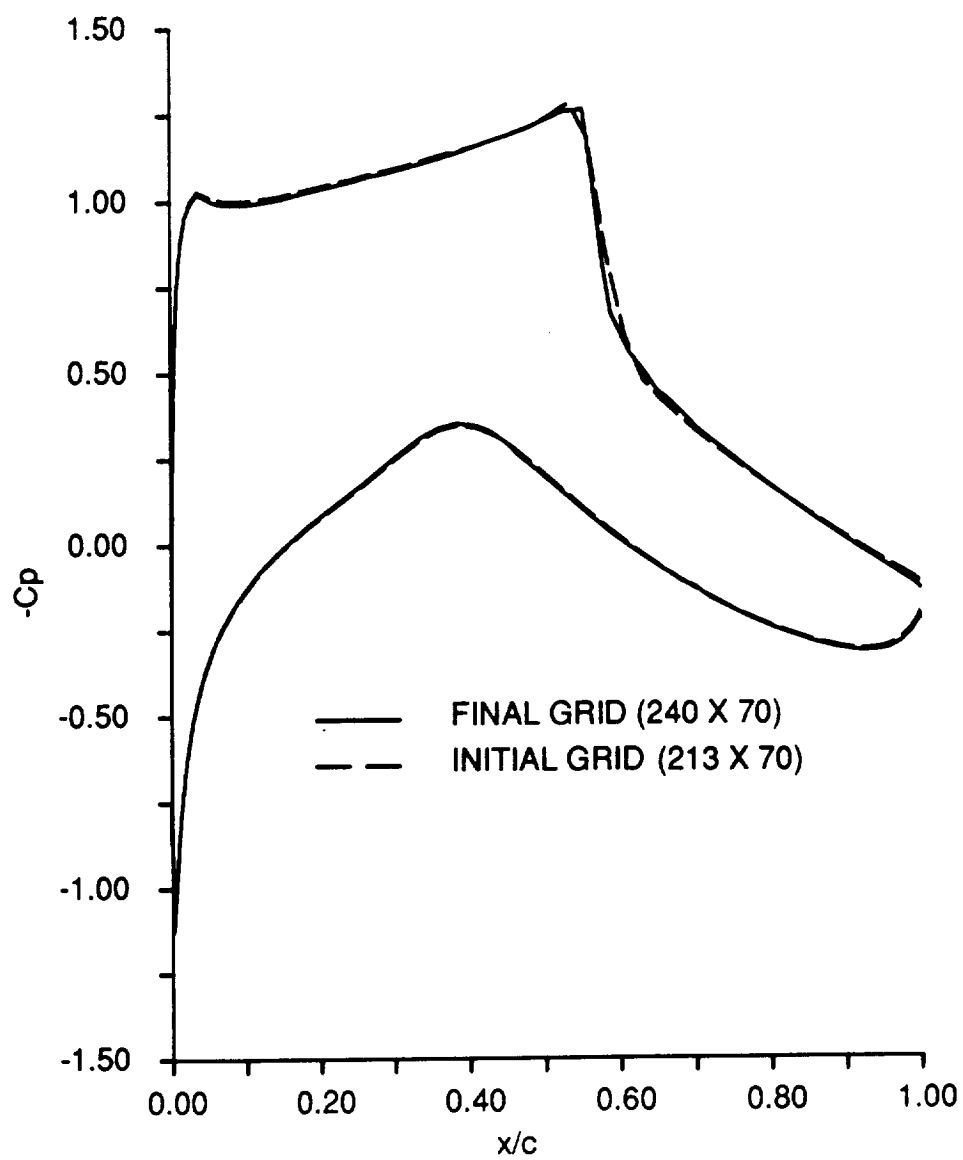


Figure 5.19: RAE 2822: effect of grid at $M_\infty = 0.75$, $Re = 6.2 \times 10^6$, $\alpha_{comp} = 2.80^\circ$, $\alpha_{exp} = 3.19^\circ$

The Langley 6- by 28-inch blowdown transonic tunnel was used to test airfoil A 153W. The airfoil model had a four inch chord and an aspect ratio of 1.50. A total pressure wake survey probe located 2.75 chords downstream from the trailing-edge was used for the calculation of C_d . Surface pressures were integrated to obtain C_n . The flow was tripped on both the upper and the lower surfaces at 6% of chord. The experimental angle of attack mentioned in Reference [4] included corrections for lift interference.

Results from two flow configurations, one subcritical and the other supercritical, are presented here and summarized in Table 5.3. The numerical grid contained 221×92 grid cells. Twenty-five of the cells in the η direction were packed in one-half of the blunt trailing-edge region.

The first Integrated Technology airfoil calculation corresponds to a Mach number of 0.602, experimental and computational angles of attack of 0.82° and a Reynolds number of 6×10^6 . Figure 5.21 shows the comparison between the computational and experimental surface-pressure coefficients. Excellent agreement between the pressure coefficients is observed. The predicted lift, drag and pitching moment coefficients are 0.3986, 0.00973 and -0.0737, respectively, which compare well with the corresponding experimental values of 0.3651, 0.0096 and -0.0619. In this case, there is no separation and no supersonic regions. The pressure contour plot is shown in Figure 5.22.

The second Integrated Technology airfoil calculation corresponds to a Mach number of 0.725, experimental and computational angles of attack of 1.65° and a Reynolds number of 3×10^6 . There was a large separation region on the upper surface and the numerical solution indicated large amplitude unsteadiness. The flow on the up-

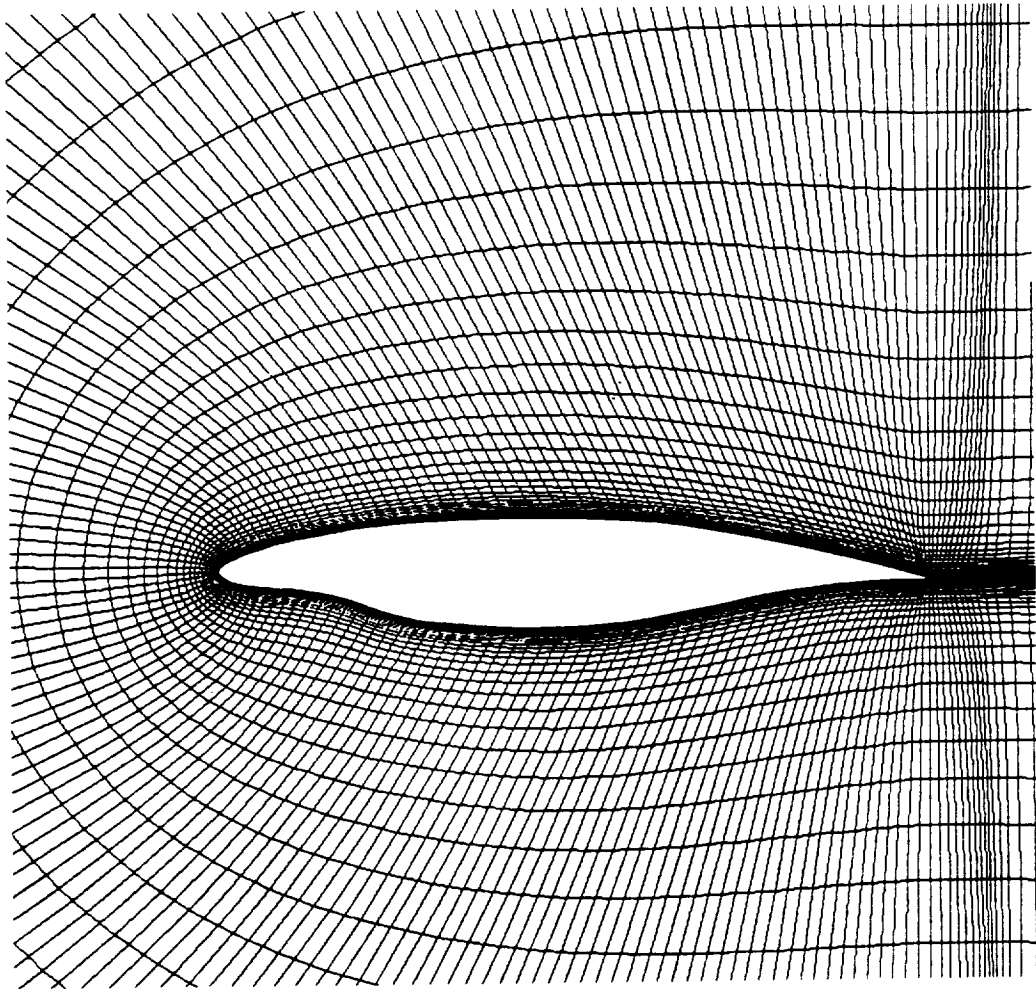


Figure 5.20: Integrated Technology airfoil A 153W grid

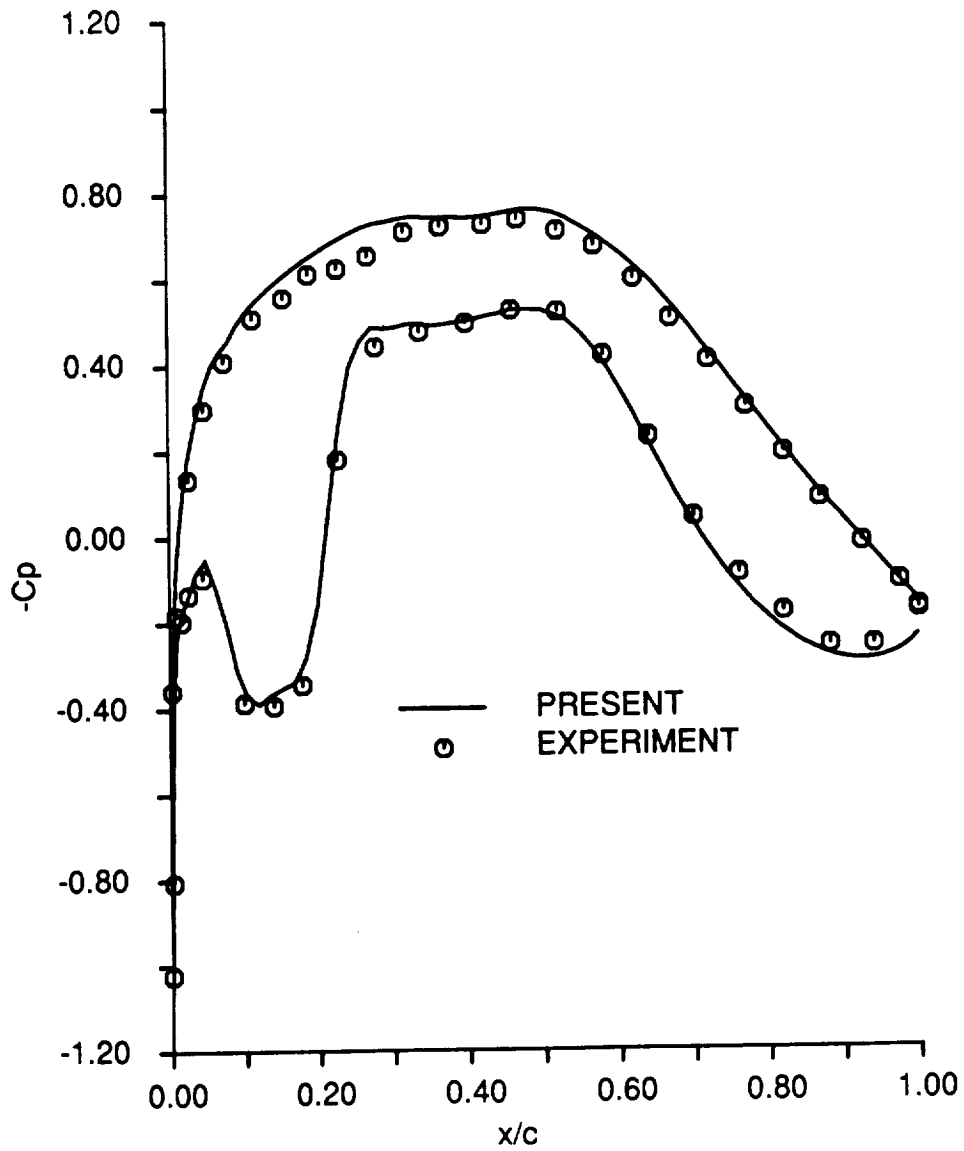


Figure 5.21: Integrated Technology A 153W: surface-pressure coefficient at $M_\infty = 0.602$, $Re = 6.0 \times 10^6$, $\alpha_{comp} = 0.82^\circ$, $\alpha_{exp} = 0.82^\circ$

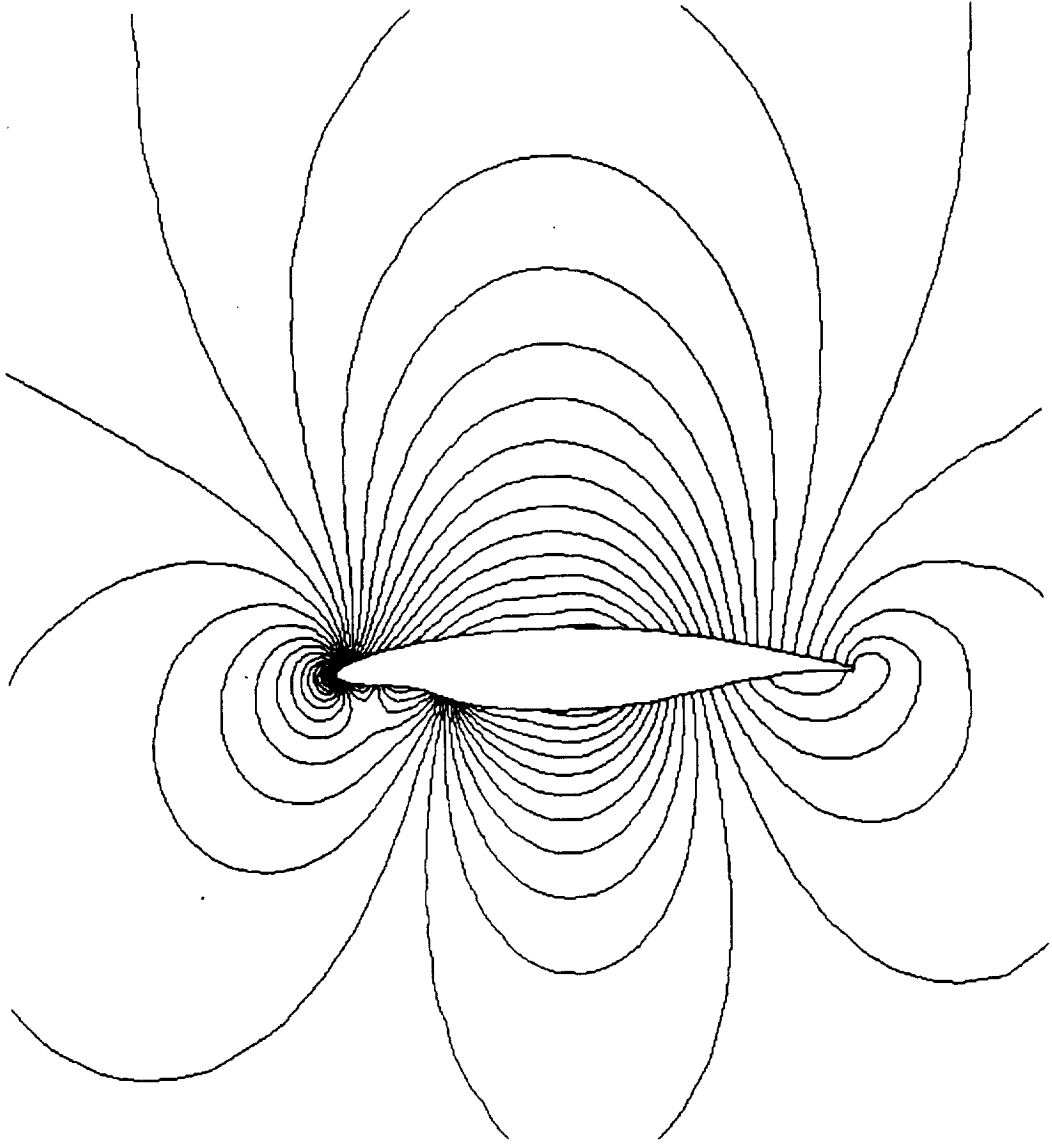


Figure 5.22: Integrated Technology A 153W: pressure contours at $M_\infty = 0.602$,
 $Re = 6.0 \times 10^6$, $\alpha_{comp} = 0.82^\circ$, $\alpha_{exp} = 0.82^\circ$

Table 5.3: Experimental and Computed Force Coefficients of A 153W Airfoil

M_∞	$Re \times 10^{-6}$	Computation			Experiment		
		α	C_l	C_d	α	C_l	C_d
0.602	6.0	0.82	0.3986	0.0097	0.82	0.3651	0.0096
0.725	3.0	1.65	0.4394	0.0176	1.65	0.4378	0.0163

per surface separated at about 25% chord downstream of the shock wave and never reattached. Distinct periodicity in the computational results was observed and the results corresponding to a minimum change in the flow variables between successive iteration levels were taken to be the final solution. Figure 5.23 shows the comparison between the computational and experimental surface-pressure coefficients. Excellent agreement between computational and experimental pressure coefficients is observed and the shock location is correctly predicted. The skin-friction distribution on the upper surface is portrayed in Figure 5.24 which shows trailing-edge separation. The predicted lift, drag and pitching moment coefficients are 0.4395, 0.0176 and -0.0606, respectively, which are in close agreement with the corresponding experimental values of 0.4378, 0.0163 and -0.0537. The pressure contour plot and the Mach number contour plots are shown in Figures 5.25 and 5.26 respectively.

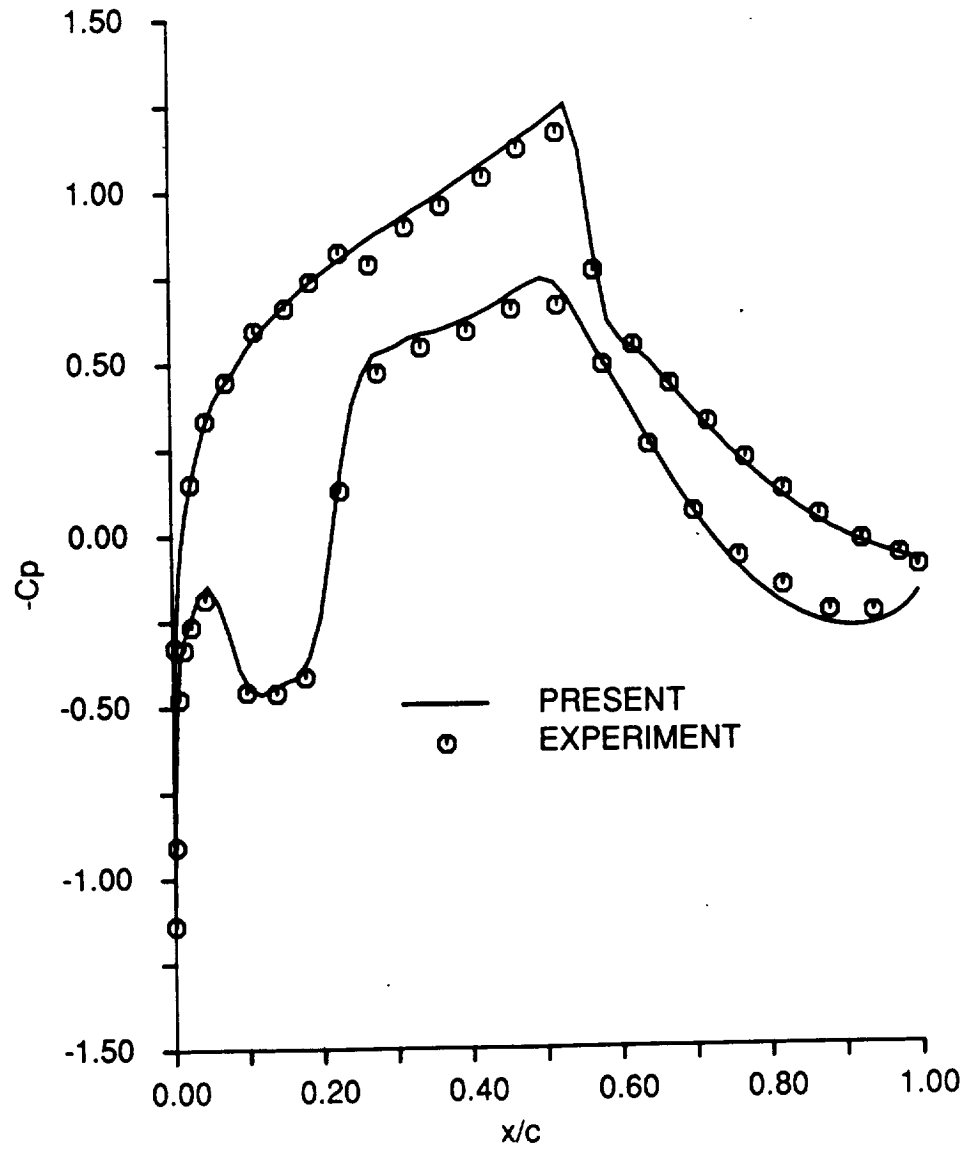


Figure 5.23: Integrated Technology A 153W: surface-pressure coefficient at $M_\infty = 0.725$, $Re = 3.0 \times 10^6$, $\alpha_{comp} = 1.65^\circ$, $\alpha_{exp} = 1.65^\circ$

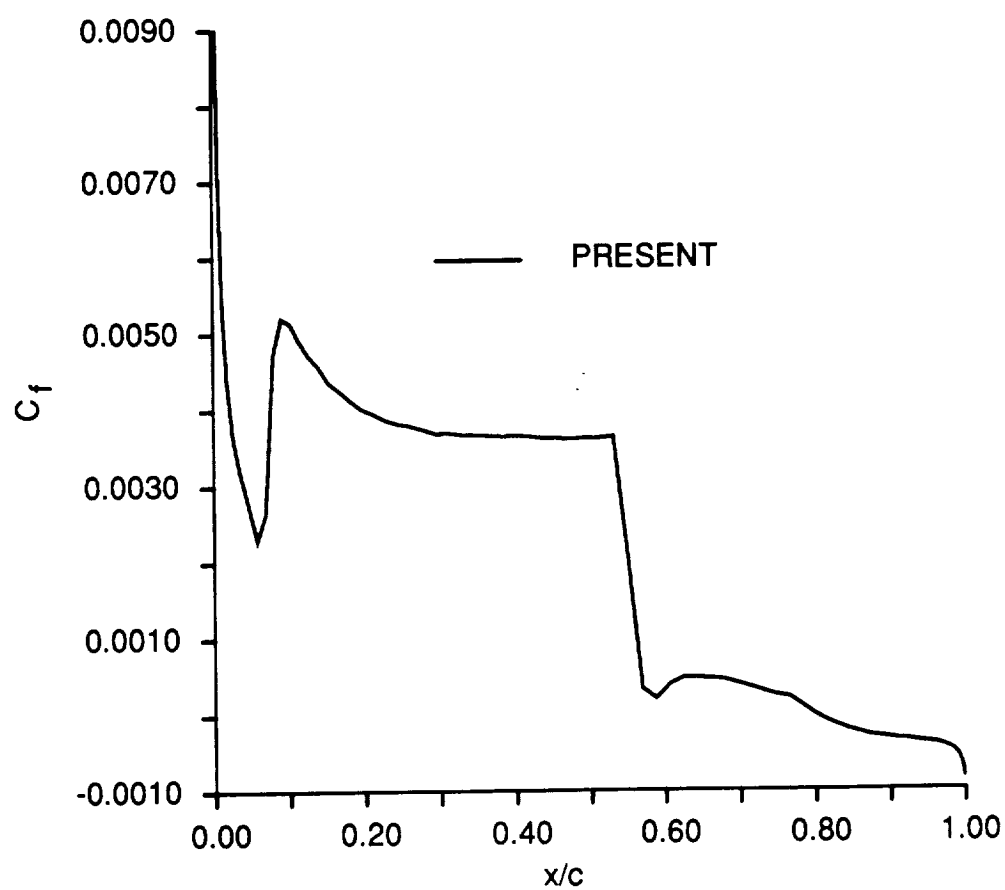


Figure 5.24: Integrated Technology A 153W: skin-friction coefficient at $M_\infty = 0.725$, $Re = 3.0 \times 10^6$, $\alpha_{comp} = 1.65^\circ$, $\alpha_{exp} = 1.65^\circ$

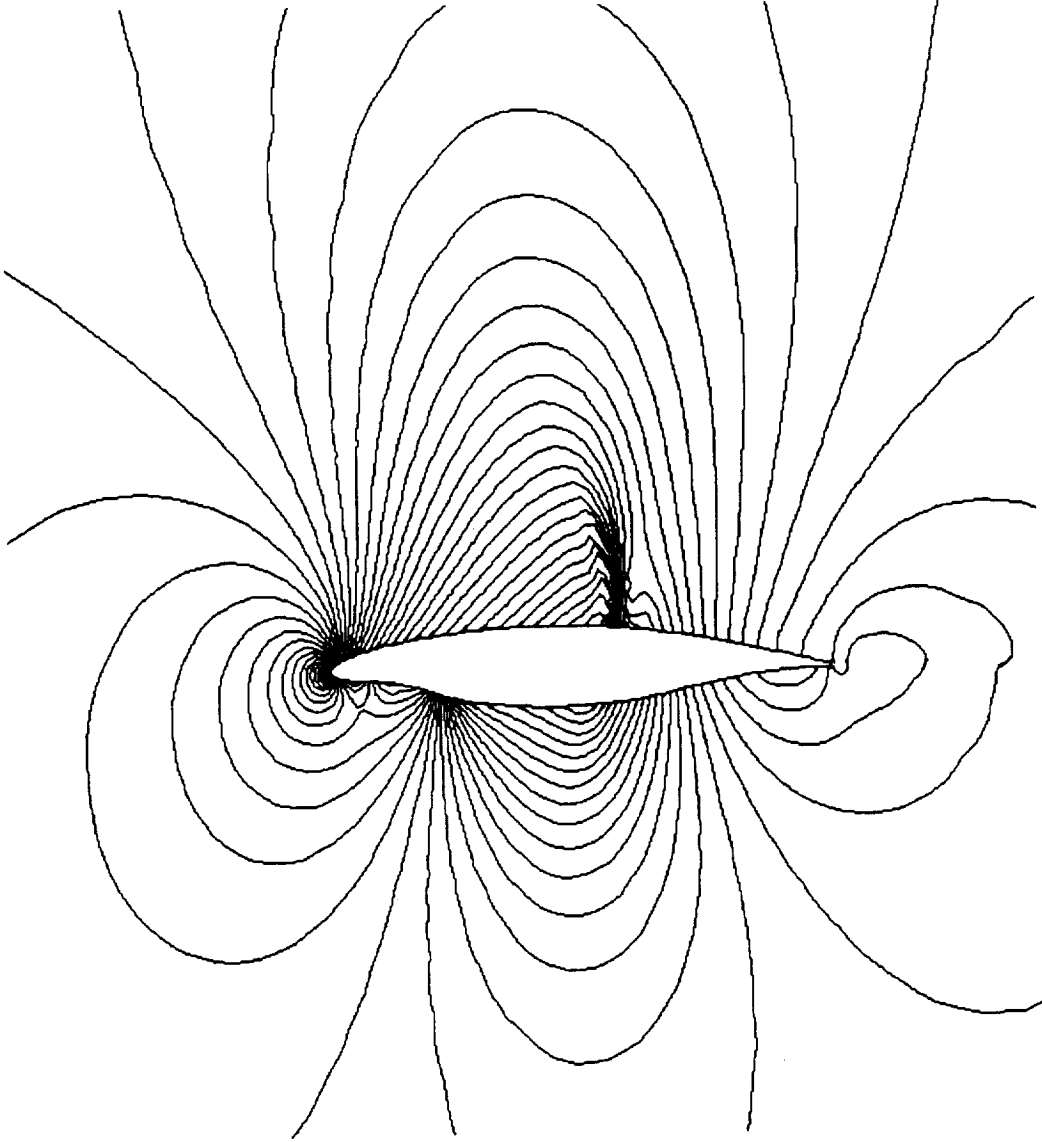


Figure 5.25: Integrated Technology A 153W: pressure contours at $M_\infty = 0.725$,
 $Re = 3.0 \times 10^6$, $\alpha_{comp} = 1.65^\circ$, $\alpha_{exp} = 1.65^\circ$

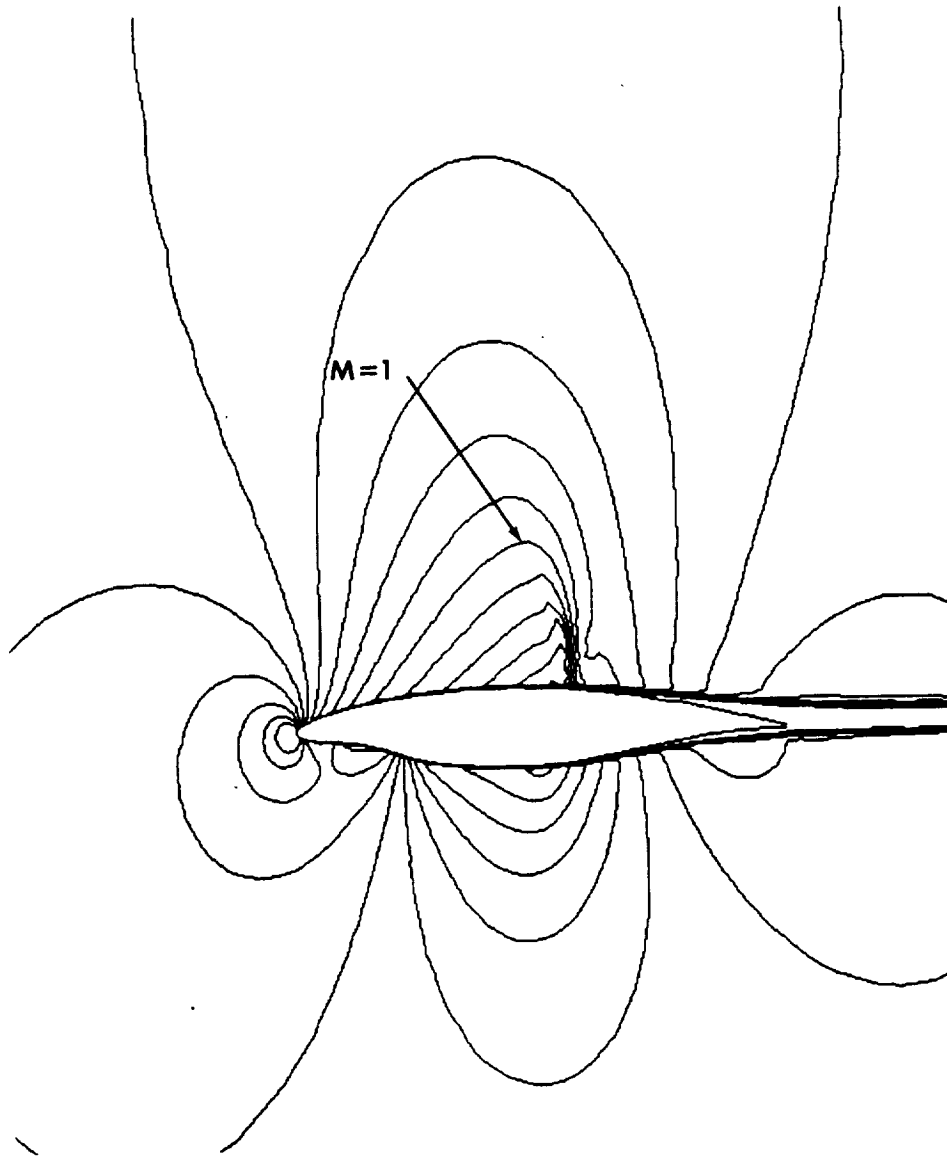


Figure 5.26: Integrated Technology A 153W: Mach number contours at $M_\infty = 0.725$, $Re = 3 \times 10^6$, $\alpha_{comp} = 1.65^\circ$, $\alpha_{exp} = 1.65^\circ$

CHAPTER 6. CONCLUDING REMARKS

A new nonequilibrium turbulence model has been developed for computation of wall bounded two-dimensional turbulent flows. The model, which is patterned after the Johnson-King model [12], is based on the turbulent kinetic energy equation and available experimental results for both attached and separated flows. Performance of this model was tested by solving the Reynolds time-averaged Navier-Stokes equations for various flow conditions around three different airfoil shapes. No changes were made in the model parameters while different test cases were being considered.

Based on the results obtained, both the attached and the shock-induced separated flow cases compare closely with the experimental data. One exception is the NACA 0012 separated flow case, where the pressure on the lower surface is slightly underpredicted; though not as much as the Johnson-King model [12]. It is felt that this small difference is due to the modeled form of the turbulence diffusion term. Further study on the diffusion term and the inner-layer turbulence velocity scale is currently being performed to understand the phenomenon better. Finally, since unsteadiness was observed for cases with large regions of separation, the model should be tested further by incorporating it into other existing Navier-Stokes codes.

BIBLIOGRAPHY

- [1] Holder, D. W., Pearcey, H. H. and Gadd, G. E. The Interaction Between Shock Waves and Boundary Layers. Aeronautical Research Council C. P. No. 180 (16,526), 1955.
- [2] Liebeck, R. H. A Class of Airfoils Designed for High Lift in Incompressible Flow. *Journal of Aircraft*, 10, No. 10 (1973): 610-617.
- [3] Harvey, W. D. and Pride, J. D. The NASA Langley Laminar Flow Control Airfoil Experiment. AIAA Paper No. 82-0567, March 1982.
- [4] Morgan, H. L., Sewall, W. G., Schumacher, M. C. and Boyd, C. N. Compilation of Data from Tests of Five Boeing Integrated Technology (IT) Airfoils in the Langley 6- by 28-Inch Transonic Tunnel. NASA TM-86419, Parts I and II, 1985.
- [5] Pearcey, H. H. The Aerodynamic Design of Section Shapes for Swept Wings. In *Advances in Aeronautical Sciences*. Vol. 3. Pergamon Press, London, 1962.
- [6] Holder, D. W. The Transonic Flow Past Two-Dimensional Airfoils. *Journal of the Royal Aeronautical Society*, 68 (August 1964): 501-516.
- [7] Pollock, N. Transonic Wind Tunnel Tests on Two Blunt Trailing Edge Aerofoils. Aerodynamics Note 351. Department of Defence, Australian Defence Scientific Service, Aeronautical Research Laboratories, 1974.
- [8] Cox, R. A. Navier-Stokes Solutions of 2-D Transonic Flow over Unconventional Airfoils. Ph.D. Thesis, Iowa State University, 1989.
- [9] Holst, T. L. Viscous Transonic Airfoil Workshop Compendium of Results. AIAA Paper No. 87-1460, June 1987.
- [10] Bradshaw, P. The Understanding and Prediction of Turbulent Flow. *Aeronautical Journal*, 76 (July 1972): 403 - 418.
- [11] Bradshaw, P. and Ferriss, D. H. Nat. Phys. Lab. Aero. Report No. 1145, 1965.

- [12] Johnson, D. A. and King, L. S. A Mathematically Simple Closure Model for Attached and Separated Turbulent Boundary Layers. *AIAA Journal*, 23, No. 11 (1985): 1684 - 1692.
- [13] Townsend, A. A. *The Structure of Turbulent Shear Flow*, Cambridge University Press, Cambridge, England, 1956.
- [14] Cebeci, T. and Smith, A. M. O. *Analysis of Turbulent Boundary Layers*. Academic Press, New York, 1974.
- [15] Anderson, D. A., Tannehill, J. C. and Pletcher, R. H. *Computational Fluid Dynamics and Heat Transfer*. McGraw-Hill/ Hemisphere, New York, 1984.
- [16] Keenan, J. H., Chao, J. and Kaye, J. *Gas Tables*. Second Edition. John Wiley and Sons, New York, 1980.
- [17] Bradshaw, P., Ferriss, D. H. and Atwell, N. P. Calculations of Boundary Layer Development Using the Turbulent Energy Equation. *Journal of Fluid Mechanics*, 28, Pt. 3 (1967): 593-616.
- [18] Rubesin, M. W. Numerical Turbulence Modelling. AGARD LS-86, 1977.
- [19] Simpson, R. L. Two-Dimensional Turbulent Separated Flow. AGARDograph No. 287, Vol. 1, 1985.
- [20] Baldwin, B. S. and Lomax, H. Thin Layer Approximation and Algebraic Model for Separated Turbulent Flows. AIAA Paper No. 78-257, January 1978.
- [21] Stock, H. W. and Hasse, W. Determination of Length Scales in Algebraic Turbulence Models for Navier-Stokes Methods. *AIAA Journal*, 27, No. 1 (1989): 5-14.
- [22] Ramaprian, B. R. and Patel, V. C. The Symmetric Turbulent Wake of a Flat Plate. *AIAA Journal*, 20, No. 9 (1982): 1228-1235.
- [23] Townsend, A. A. The Fully Developed Turbulent Wake of a Circular Cylinder. *Australian Journal of Scientific Research, Series A*, 2 (1949): 451-468.
- [24] Rodi, W. A Review of Experimental Data of Uniform-Density Free Turbulent Boundary Layers. *Studies in Convection*. Vol. 1. Edited by B. E. Launder. Academic Press, New York, 1975.
- [25] Ramaprian, B. R., Patel, V. C. and Sastry, M. S. Turbulent Wake Development Behind Streamlined Bodies. Institute of Hydraulic Research. University of Iowa. IHR Report 231, 1981.

- [26] Bradshaw, P. Prediction of the Turbulent Near-Wake of a Symmetrical Airfoil. AIAA Journal, 8, No. 8 (1970): 1507-1508.
- [27] Townsend, A. A. The Flow in a Turbulent Boundary Layer after a Change in Surface Roughness. Journal of Fluid Mechanics, 26 (1966): 255.
- [28] Cebeci, T. and Meier, H. U. Modelling Requirements for the Calculation of Turbulent Flow around Airfoils, Wings and Bodies of Revolution. Turbulent Boundary Layers: Experiments, Theory and Modelling, AGARD-CP-271, January 1980, p. 181.
- [29] Roe, P. L. Approximate Riemann Solvers, Parameter Vectors and Difference Schemes. Journal of Computational Physics, 43 (1981): 357-372.
- [30] Chakravarthy, S. R. and Osher, S. A New Class of High Accuracy TVD Schemes for Hyperbolic Conservation Laws. AIAA Paper No. 85-0363, January 1985.
- [31] Chakravarthy, S. R., Szema, K-Y., Goldberg, U. C., Gorski, J. J. and Osher, S. Application of a New Class of High Accuracy TVD Schemes to the Navier-Stokes Equations. AIAA Paper No. 85-0165, January 1985.
- [32] Yee, H. C., Warming, R. F. and Harten, A. Implicit Total Variation Diminishing (TVD) Schemes for Steady-State Calculations. AIAA Paper No. 83-1902, 1983.
- [33] Sorensen, R. L. A Computer Program to Generate Two-Dimensional Grids About Airfoils and Other Shapes by the Use of Poisson's Equation. NASA TM-81198, 1980.
- [34] Harris, C. D. Two-Dimensional Aerodynamic Characteristics of the NACA 0012 Airfoil in the Langley 8-Foot Transonic Pressure Tunnel. NASA TM-81927, 1981.
- [35] Cook, P. H., McDonald, M. A. and Firmin, M. C. P. AEROFOIL RAE 2822 Pressure Distributions, and Boundary Layer and Wake Measurements. AGARD Advisory Report No. 138, 1979.
- [36] Coakley, T. J. Numerical Simulation of Viscous Transonic Airfoil Flows. AIAA Paper No. 87-0416, January 1987.
- [37] Coles, D. The Law of the Wake in Turbulent Boundary Layer. Journal of Fluid Mechanics, 1, Pt. 2 (Feb. 1956): 191-226.

ACKNOWLEDGEMENTS

This research was supported by NASA Langley Research Center under Grant NAG-1-645 through funds provided by the Office of Naval Research. The Technical Monitors for this research have been W. G. Sewall and W. D. Harvey. The authors wish to acknowledge the contribution of R. A. Cox in developing the numerical algorithm used in this study and to thank R. G. Rajagopalan for his helpful suggestions.

APPENDIX A. TURBULENT DIFFUSION

The turbulent diffusion term is patterned after Johnson and King [12]. As a starting point, the bulk convection hypothesis of Townsend [13], namely

$$\frac{\partial D_s}{\partial y} = \frac{\partial}{\partial y}(\bar{k}V) \quad (\text{A.1})$$

is used. Here V is a lateral convection velocity representing the turbulent transport by more energetic large eddies. Along the path of maximum $y\tau$,

$$\left(\frac{\partial D_s}{\partial y}\right)_m = \frac{(y\tau)_m}{a_1} \frac{\partial}{\partial y} \left(\frac{V}{y}\right)_m \quad (\text{A.2})$$

where the relationship $\overline{-u'v'}/\bar{k} = a_1$ has been applied. The approximate model for the variation of V with y/δ suggested by Johnson and King [12] is utilized here to obtain

$$\frac{\partial}{\partial y} \left(\frac{V}{y}\right) \Big|_m = \left(\frac{V_o}{0.7\delta - y_{max}}\right) \left(\frac{y_{max}}{y_m^2}\right) \quad (\text{A.3})$$

V_o mentioned in the foregoing equation is the maximum lateral convection velocity which is assumed to occur at $y \simeq 0.7\delta$. V_o is expected to be proportional to the maximum turbulent shear stress, i.e.,

$$V_o = C_{model}(\tau_{max})^{1/2}$$

It is to be noted here that the additional restriction on V_o placed by Johnson and King, namely

$$V_o \propto (\tau_{max})^{1/2} \left[1 - \left(\frac{dissipation}{production} \right)_o \right]$$

has been dropped here. This is because it is believed here that in the case of equilibrium turbulence, the diffusion term is balanced by the convection term in the turbulent kinetic energy equation; not that the diffusion term is independently zero. Thus equation A.2 with the aid of A.3 becomes

$$\left(\frac{\partial D_s}{\partial y} \right)_m = \frac{C_{model} \tau_m \tau_{max}^{1/2} y_{max}}{a_1 (0.7\delta - y_{max}) y_m} \quad (A.4)$$

APPENDIX B. NONEQUILIBRIUM EFFECTS IN THE INNER LAYER

Based on the assumption that the Coles velocity profiles [37] describe turbulent mean flows of attached and slightly separated boundary layers, it is possible to deduce a relationship between the turbulence velocity scales in the inner and the outer regions of such shear layers. Using Hinze's expression for the universal wake function, the Coles velocity profiles in defect form is written as

$$\frac{U_e - \bar{u}}{U_e} = \frac{\sigma}{\kappa} \left[\text{sign}(\sigma) \Pi \left\{ 1 + \cos\left(\pi \frac{y}{\delta}\right) \right\} - \ln \frac{y}{\delta} \right] \quad (\text{B.1})$$

where

$$\sigma = \frac{|c_f|}{c_f} \left[\frac{|c_f|}{2} \right]^{1/2} = \text{sign}(\tau_w) \frac{u\tau}{U_e} \left[\frac{\rho_w}{\rho_e} \right]^{1/2}$$

Differentiating B.1 with respect to y one obtains,

$$y \left| \frac{\partial \bar{u}}{\partial y} \right| = \frac{U_e |\sigma|}{\kappa} \left[\pi \Pi \frac{y}{\delta} \sin \left(\pi \frac{y}{\delta} \right) + \frac{\sigma}{|\sigma|} \right] \quad (\text{B.2})$$

Since the law of the wall delivers $\kappa y \left| \frac{\partial u}{\partial y} \right| = \sigma U_e = \text{constant}$, σU_e can be interpreted as the turbulence velocity scale V_{s_i} in the inner layer. The y location for the maximum

value of $y \frac{\partial u}{\partial y}$, as observed from equation B.2, is 0.646δ . With these identifications, and replacing $\partial \bar{u}/\partial y$ with ω , equation B.2 may be rewritten as

$$V_{s_i} = \frac{\kappa(y | \omega |)_{max_F}}{1 + 1.82\Pi} \quad (B.3)$$

For equilibrium turbulent flow, $(y | \omega |)_{max_F}$ is proportional to the turbulence velocity scale V_{s_o} in the outer layer. Equation B.3 thus yields a relationship between the inner and the outer turbulence velocity scales.

$$V_{s_i} = \frac{\kappa(constant)V_{s_o}}{1 + 1.82\Pi} \quad (B.4)$$

It is now hypothesized that the above relationship holds for nonequilibrium turbulence as well. Since g_e/g can be interpreted as a nonequilibrium correction applied to V_{s_o} ,

$$V_{s_i} = \frac{\kappa(constant)V_{s_o,e}g_e/g}{1 + 1.82\Pi} \quad (B.5)$$

Finally, writing Π in terms of $(y | \omega |)_{max_F}$ with the aid of equation B.2 and identifying this vorticity function with the equilibrium outer turbulence velocity scale, one obtains

$$V_{s_i} = V_{s_{i,e}} F_c \quad (B.6)$$

with

$$F_c = \frac{g_e/g}{1 - f_1} \quad (\text{B.7})$$

$$f_1 = \frac{u_\tau(\rho_w/\rho_e)^{1/2}(\tau_w/|\tau_w|)[1 - \tau_w/|\tau_w|]}{\kappa F_{max}} \quad (\text{B.8})$$

where $V_{s_{i,e}} = \sigma U_e$ has been used.

